

Central Lancashire Online Knowledge (CLoK)

| | |
|----------|------------------------------------------------------------------------------------------------------------------------------------------------------------------------------------------------------------------------------------------------------------------------------------------------------------------------------------------------|
| Title | Galaxy And Mass Assembly (GAMA): the wavelength-dependent sizes and profiles of galaxies revealed by MegaMorph |
| Type | Article |
| URL | https://clock.uclan.ac.uk/10937/ |
| DOI | https://doi.org/10.1093/mnras/stu632 |
| Date | 2014 |
| Citation | Vulcani, B., Bamford, S. P., Haussler, B., Vika, M., Rojas, A., Agius, N. K., Baldry, I., Bauer, A. E., Brown, M. J. I. et al (2014) Galaxy And Mass Assembly (GAMA): the wavelength-dependent sizes and profiles of galaxies revealed by MegaMorph. Monthly Notices of the Royal Astronomical Society, 441 (2). pp. 1340-1362. ISSN 0035-8711 |
| Creators | Vulcani, B., Bamford, S. P., Haussler, B., Vika, M., Rojas, A., Agius, N. K., Baldry, I., Bauer, A. E., Brown, M. J. I., Driver, S., Graham, A. W., Kelvin, L. S., Liske, J., Loveday, J., Popescu, Cristina, Robotham, A. S. G. and Tuffs, R. J. |

It is advisable to refer to the publisher's version if you intend to cite from the work.
<https://doi.org/10.1093/mnras/stu632>

For information about Research at UCLan please go to <http://www.uclan.ac.uk/research/>

All outputs in CLoK are protected by Intellectual Property Rights law, including Copyright law. Copyright, IPR and Moral Rights for the works on this site are retained by the individual authors and/or other copyright owners. Terms and conditions for use of this material are defined in the <http://clock.uclan.ac.uk/policies/>

DART-RAY: a 3D ray-tracing radiative transfer code for calculating the propagation of light in dusty galaxies

G. Natale,^{1*} C. C. Popescu,^{1,2} R. J. Tuffs² and D. Semionov¹

¹Jeremiah Horrocks Institute, University of Central Lancashire, Preston PR1 2HE, UK

²Max Planck Institute für Kernphysik, Saupfercheckweg 1, D-69117 Heidelberg, Germany

Accepted 2013 December 13. Received 2013 November 20; in original form 2013 August 14

ABSTRACT

We present DART-RAY, a new ray-tracing 3D dust radiative transfer (RT) code designed specifically to calculate radiation field energy density (RFED) distributions within dusty galaxy models with arbitrary geometries. In this paper, we introduce the basic algorithm implemented in DART-RAY which is based on a pre-calculation of a lower limit for the RFED distribution. This pre-calculation allows us to estimate the extent of regions around the radiation sources within which these sources contribute significantly to the RFED. In this way, ray-tracing calculations can be restricted to take place only within these regions, thus substantially reducing the computational time compared to a complete ray-tracing RT calculation. Anisotropic scattering is included in the code and handled in a similar fashion. Furthermore, the code utilizes a Cartesian adaptive spatial grid and an iterative method has been implemented to optimize the angular densities of the rays originated from each emitting cell. In order to verify the accuracy of the RT calculations performed by DART-RAY, we present results of comparisons with solutions obtained using the DUSTY 1D RT code for a dust shell illuminated by a central point source and existing 2D RT calculations of disc galaxies with diffusely distributed stellar emission and dust opacity. Finally, we show the application of the code on a spiral galaxy model with logarithmic spiral arms in order to measure the effect of the spiral pattern on the attenuation and RFED.

Key words: radiative transfer – scattering – dust, extinction.

1 INTRODUCTION

Interstellar dust is of primary importance in determining the spectral energy distribution (SED) of the radiation escaping from galaxies at wavelengths ranging from the ultraviolet (UV) to the submillimetre (submm) and radio. Dust attenuates and redistributes the light, originating mainly from stars and, if present, from an active galactic nucleus (AGN), by either absorbing or scattering photons. The absorbed luminosity is then re-emitted in the infrared regime. The dust may be situated in complex geometries with respect to these sources, affecting the observed structure of the galaxy at each wavelength as well as its integrated SED. Modelling the propagation of light within real galaxies is thus a challenging task. Nevertheless, it is essential to do such modelling, if physical quantities of interest, such as the distribution and properties of the stellar populations and the interstellar medium (ISM) as traced by dust and the interstellar radiation fields, are to be derived from multiwavelength images and SEDs.

Taking advantage of the approximate cylindrical symmetry of galaxies, 2D dust radiative transfer (RT) models, such as the one

presented by Popescu et al. (2011), already contain the main ingredients needed to predict integrated galaxy SEDs, average profiles, dust emission and attenuation for the case of normal star-forming disc galaxies. However, there are a number of reasons why 3D dust RT codes are desirable. First, spiral galaxies, although well modelled with 2D codes, show the presence of multiple and irregular features such as spiral structures, bars, warps and local clumpiness of the ISM. Also, galaxies may host a central AGN whose polar axis may not be aligned with that of the galaxy. For mergers or post-merger galaxies there is clearly no fundamental symmetry of the distribution of stars and dust. Finally, solutions for the distribution of stars and ISM provided by numerical simulations of forming and evolving galaxies generally require processing with a 3D RT code in order to predict the appearance in different bands.

The main challenge in realizing 3D solutions of the dust RT problem is the computational expense. The stationary 3D dust RT equation is a non-local non-linear equation: non-local in space (photons propagate within the entire domain), direction (due to scattering, absorption/re-emission) and wavelength (absorption/re-emission). Even using a relatively coarse resolution in each of the six fundamental variables, namely the three spatial coordinates, the two angles specifying the radiation direction and the wavelength, solving the 3D dust RT problem require an impressive amount of both

*E-mail: gnatale@uclan.ac.uk

memory and computational speed, at the limits of the capabilities of current computers.

Possibly the quickest way to calculate an image of a galaxy in direct and scattered light in a particular direction is by using Monte Carlo (MC) methods (including modern acceleration techniques; see Steinacker, Baes & Gordon 2013). There is a rich history of applications of MC codes to dust RT problems, starting with the pioneering works of e.g. Mattila (1970), Roark, Roark & Collins (1974), Witt & Stephens (1974) and Witt (1977). In the following decades the MC RT technique was further developed by many authors such as e.g. Witt, Thronson & Capuano (1992), Fischer, Henning & Yorke (1994), Bianchi, Ferrara & Giovanardi (1996), Witt & Gordon (1996) and Dullemond & Turolla (2000). Nowadays, this method can be considered as the mainstream approach to 3D dust RT calculations (see e.g. Gordon et al. 2001; Ercolano, Barlow & Storey 2005; Jonsson 2006; Bianchi 2008; Chakrabarti & Whitney 2009; Baes et al. 2011; Robitaille 2011, but also see table 1 of Steinacker et al. 2013 for a recent list of published 3D dust RT codes). The MC approach to dust RT consists of a simulation of the propagation of photons within a discretized spatial domain, based on a probabilistic determination of the location of emission of the photons, their initial propagation direction, the position where an interaction event (absorption or scattering) occurs and the new propagation direction after a scattering event. Thus, the MC technique mimics closely the actual processes occurring in nature which shape the appearance of galaxies in UV/optical light. However, since it is based on a probabilistic approach to determine the photon propagation directions, an RT MC calculation does not necessarily determine the radiation field energy density (RFED) accurately in the entire volume of the calculation. The reason is that regions which have a low probability of being illuminated are reached by only few photons unless the total number of photons in the RT run is substantially increased. Nonetheless, in the case of disc galaxies, accurate calculation of radiation field intensities throughout the entire volume is needed, in particular for the calculation of dust emission. Indeed, far-infrared (FIR)/submm observations of spiral galaxies show that most of the dust emission luminosity is emitted longwards of 100 μm (see e.g. Sodroski et al. 1997; Odenwald, Newmark & Smoot 1998, Popescu & Tuffs 2002; Popescu et al. 2002; Dale et al. 2007, 2012; Bendo et al. 2012) through grains situated in the diffuse ISM which are generally located at very considerable distances from the stars heating the dust.

Another method to solve the RT problem in galaxies, alternative to the mainstream MC approach, is by using a ray-tracing algorithm. This method consists in the calculation of the variation of the radiation specific intensity along a finite set of directions, usually referred to as ‘rays’. Ray-tracing algorithms can be specifically designed to calculate radiation field intensities throughout the entire volume considered in the RT calculation. Also, it should be pointed out that MC codes already make large use of ray-tracing operations (see Steinacker et al. 2013). It is thus interesting to pursue in the developing of pure ray-tracing 3D RT codes, which can be sufficiently efficient for the modelling of galaxies with 3D arbitrary geometries, if appropriate acceleration techniques are implemented. Similar to MC codes, ray-tracing dust RT codes have had a rich history in astrophysics (see e.g. Hummer & Rybicki 1971; Rowan-Robinson 1980; Efstathiou & Rowan-Robinson 1990; Siebenmorgen, Kruegel & Mathis 1992; Semionov & Vasevicius 2005, 2006). Application to analysis of galaxies started with the 2D code of Kylafis & Bahcall (1987). Although originally implemented only for the calculation of optical images (see also Xilouris et al. 1997, 1998, 1999), this algorithm was later adapted by Popescu et al. (2000) for the

calculation of radiation fields and was coupled with a dust emission model (including stochastic heating of grains) to predict the full mid-infrared (MIR)/FIR/submm SED of spiral galaxies (see also Misiriotis et al. 2001; Popescu et al. 2011). Thus far, extensions of the ray-tracing technique to 3D have been implemented but are specifically designed for solving the RT problem for star-forming clouds (e.g. Steinacker et al. 2003; Kuiper et al. 2010), heated by few dominant discrete sources, rather than for very extended distributions of emission and dust as encountered in galaxies.

In this paper, we present *DART-RAY*,¹ a new ray-tracing algorithm which is optimized for the solution of the 3D dust RT problem for galaxies with arbitrary geometries and moderate optical depth at optical/UV wavelengths.² The main challenge faced by this model is the construction of an efficient algorithm for the placing of rays throughout the volume of the galaxy. In fact, a complete ray-tracing calculation between all the cells, used to discretize a model, is not a viable option, since it is by far too computationally expensive even for relatively coarse spatial resolution. Our algorithm circumvents the problem by performing an appropriate pre-calculation, whose goal is to provide a lower limit to the RFED distribution throughout the model. In this way, the ray angular density needed in the actual RT calculation can be dynamically adjusted such that the ray contributions to the local RFED are calculated only within the fraction of the volume where these contributions are not going to be negligible.

Furthermore, the code we developed can be coupled with any dust emission model. Applications of the 3D code for calculation of infrared emission from stochastically heated dust grains of various sizes and composition, including heating of polycyclic aromatic hydrocarbons (PAH) molecules, utilizes the dust emission model from Popescu et al. (2011), and will be given in a future paper.

The paper is structured as follows. In Section 2 we provide some background information and motivation behind our particular ray-tracing solution strategy. In Section 3 we give a technical description of our code. In Section 4 we provide some notes on implementation and performance of the code. In Section 5 we compare solutions provided by our code with those calculated by the 1D code *DUSTY* and the 2D RT calculations performed by Popescu et al. (2011). In Section 6 we show the application of the code on a galaxy model including logarithmic spiral arms. A summary closes the paper. A list of definitions for the terms and expressions used throughout the paper can be found in Table 1.

2 BACKGROUND AND MOTIVATIONS

In this section we describe the basic characteristics of the time-independent 3D dust RT equation, briefly introduce the ray-tracing approach used in our code and provide the main motivations behind our solution strategy. Finally, we describe the main steps of the new algorithm we present in this work. A much more technical description of our code can be found in Section 3.

2.1 Dust continuum 3D radiative transfer: ray tracing and solution strategy

Given an input distribution of stellar luminosity and dust mass, solving the RT problem requires in principle the resolution of the

¹ The name of the code can be seen as the acronym for ‘Dust Adaptive Radiative Transfer Ray-tracing.’

² The actual version of the code does not consider the dust absorption/scattering of light emitted by dust at other positions (so-called dust self-heating). This effect can be neglected in case the galaxies are optically thin at infrared wavelengths.

Table 1. Table of terms and definition. The subscript λ denotes a dependence from the wavelength of the radiation.

| Term | Definition |
|----------------------------------------|-----------------------------------------------------------------------------------------------------------------------------------------------------------------------------------------------------------------------------|
| A_{EM} | Projected area of an emitting cell |
| A_{INT} | Projected area of an intersected cell |
| f_L | Input parameter needed to set the threshold value for ΔL_λ below which scattering iterations are stopped |
| f_U | Input parameter needed to set the threshold value for δU_λ below which rays are stopped |
| g_λ | Henye–Greenstein scattering phase function parameter |
| I_λ | Radiation specific intensity |
| $\langle I_\lambda \rangle$ | Average of I_λ over the path crossed by a ray within an intersected cell |
| $I_{\lambda,i}$ | Radiation specific intensity of a ray before crossing a cell i |
| $I_{\lambda,esc}$ | Radiation specific intensity of a ray once it has reached the model border |
| $I_{\lambda,ext}$ | Amount of radiation specific intensity of a ray extincted within an intersected cell |
| $\delta I_{\lambda,sca}(\theta, \phi)$ | Ray contribution to the specific intensity of the radiation scattered into direction (θ, ϕ) , see Fig. 6 |
| j_λ | Volume emissivity, that is, the luminosity emitted at a certain position per unit volume, unit solid angle and unit wavelength interval (also $j_{\lambda,c}$ when referred to the average volume emissivity within a cell) |
| κ_λ | Dust extinction coefficient per unit dust mass (also $\kappa_{\lambda,abs}$ or $\kappa_{\lambda,sca}$ when referred to the extinction coefficients due to dust absorption or scattering) |
| L_λ | Total stellar luminosity density of the model |
| ΔL_λ | Amount of luminosity still to be processed during scattering iterations |
| $L_{\lambda,ray}$ | Luminosity associated with a ray beam |
| N_{rays} | Input parameter specifying the minimum number of rays crossing a cell within the fully sampled region |
| Φ_λ | Scattering phase function |
| ρ | Dust mass density (also ρ_c when referred to the average dust mass density within a cell) |
| Δr | Ray path within an intersected cell |
| SCATT_EN(θ, ϕ) | Array storing the luminosity of the radiation scattered by dusty cells into a finite set of solid angles |
| τ_λ | Optical depth |
| U_λ | RFED |
| δU_λ | Contribution to the local RFED carried by a ray (also $U_{\lambda,INT}$ when referred to the contribution to an intersected cell RFED) |
| $U_{\lambda,LL}$ | Lower limit to the RFED |
| U_{TEMP} | Temporary array used to store RFED contributions from an emitting cell throughout the model |
| $U_{\lambda,FINAL}$ | Array storing the RFED distribution which is output by the code |
| V_{INT} | Intersected cell volume |
| ω_λ | Albedo |
| $\Omega_{HP,EM}$ | Solid angle associated with the HEALPix spherical pixels used to define the directions of rays from an emitting cell |
| $\Omega_{HP,INT}$ | Solid angle associated with the HEALPix spherical pixels used to define the directions of the radiation scattered by an intersected cell |
| $\Omega_{HP,MS}$ | Solid angle associated with an HEALPix main sector (see Fig. 4) |
| Ω_{INT} | Solid angle subtended by projected area of the intersected cell A_{INT} (see Fig. 6) |
| ‘Dusty cell’ | A cell where the average value of dust density is higher than zero |
| ‘Dust self-heating’ | The dust absorption of radiation emitted by dust at other positions (not included in this version of the code) |
| ‘Emitting cell’ | A cell where the average value of the stellar light or scattered light volume emissivity is higher than zero |
| ‘Escaping radiation’ | The direct or scattered stellar radiation propagating outside the borders of the volume considered in the RT calculation |
| ‘Full sampling’ (of a region) | The process of launching enough rays from a source, such that all the cells within a region are intersected by multiple rays |
| ‘Intersected cell’ | A cell intersected by a ray |
| ‘Leaf cell’ | A cell of the 3D adaptive grid which is not further subdivided |
| ‘Lost luminosity’ | Amount of stellar luminosity not considered in the RT calculation (to be kept low to guarantee approximate energy balance, see Section 4) |
| MC | Monte Carlo |
| RFED | RFED |
| RT | Radiative transfer |
| ‘Source influence volume’ | The fraction of model volume within which a source contributes significantly to the RFED |
| ‘Volume emissivity’ | See j_λ |

following equation for the specific intensity $I(\lambda, \mathbf{x}, \mathbf{n})$, which represents the luminosity per unit area, solid angle and wavelength interval propagating at point \mathbf{x} into the direction \mathbf{n} :

$$\mathbf{n} \cdot \nabla_{\mathbf{x}} I_\lambda(\mathbf{x}, \mathbf{n}) = -k_\lambda(\mathbf{x})\rho(\mathbf{x}) \left[I_\lambda(\mathbf{x}, \mathbf{n}) - \omega_\lambda \int_{\Omega} \Phi_\lambda(\mathbf{n}, \mathbf{n}') I_\lambda(\mathbf{x}, \mathbf{n}') d\Omega' \right] + j_\lambda(\mathbf{x}), \quad (1)$$

where $k_\lambda(\mathbf{x})$ is the total extinction coefficient per unit mass of dust (including both absorption and scattering), $\rho(\mathbf{x})$ is the dust mass

density, ω_λ is the albedo, defined such that $\omega_\lambda \times k_\lambda(\mathbf{x})$ gives the fraction of extinction due to scattering, $\Phi_\lambda(\mathbf{n}, \mathbf{n}')$ is the scattering phase function, which gives the probability for radiation coming from direction \mathbf{n}' to be scattered into direction \mathbf{n} and $j_\lambda(\mathbf{x})$ is the distribution of stellar volume emissivity.³ The first term on the

³ Throughout the text by ‘volume emissivity’ we will always mean the luminosity per unit volume per unit solid angle and per unit wavelength interval of the stellar radiation at each position. To not be confused with the emissivity coefficient used to characterize the emission properties of e.g. gas or dust.

right-hand side of equation (1) acts to reduce the radiation specific intensity $I(\lambda, \mathbf{x}, \mathbf{n})$ by a quantity that is proportional to the radiation intensity itself. The second term instead acts as a source term and gives a positive contribution to the radiation intensity by adding the light coming from all directions to point \mathbf{x} and then scattered into the direction \mathbf{n} . The third term gives a positive contribution to the propagating radiation specific intensity, which is due to stellar emission and it is assumed to be isotropic at each position \mathbf{x} . Since in 3D RT there are six independent variables, namely wavelength, three spatial coordinates and two angular directions, the solution vector for $I_\lambda(\mathbf{x}, \mathbf{n})$ can be extremely large, making the problem very challenging also from the point of view of memory requirements, apart from the difficulty of solving the integrodifferential equation itself in three dimensions. Note also that we did not include a term that represents the re-emission by dust, important at infrared wavelengths. The resolution algorithm presented in this work is designed only to handle the propagation of direct and scattered light from stellar populations and does not consider the self-heating of dust.

Instead of seeking to obtain a solution for $I_\lambda(\mathbf{x}, \mathbf{n})$, the main aim of this work is to construct an algorithm optimized to derive the RFED U_λ at each position \mathbf{x} , in order to be able to calculate successively the dust emission spectra assuming local energy balance between dust radiative heating and emission.⁴

In terms of $I_\lambda(\mathbf{x}, \mathbf{n})$, one can express U_λ as

$$U_\lambda(\mathbf{x}) = \frac{\int I_\lambda(\mathbf{x}, \mathbf{n}) d\Omega}{c}. \quad (2)$$

In order to calculate $U_\lambda(\mathbf{x})$ at a specific point \mathbf{x} , one can simply sum up the contributions δU_λ provided by the radiation coming from all the emitting sources to the value of $U_\lambda(\mathbf{x})$ at that position. A numerical method to calculate $U_\lambda(\mathbf{x})$ at any position can be implemented by considering ‘rays’ originating from each emitting source and propagating throughout the whole volume considered in the calculation. Along each ray path one follows the variation of the radiation intensity and one can thus calculate the δU_λ contributions at a finite set of positions (this solution technique is among those known as ‘ray-tracing’ methods). More specifically, a solution algorithm one could use to derive the distribution of $U_\lambda(\mathbf{x})$ for a single wavelength λ , given an input 3D distribution of stellar luminosity and dust mass, is the following.

First, the entire model is subdivided in an adaptive grid of cubic cells and to each cell one assigns the average values for both the dust density and stellar volume emissivity within the cell volume. A cell for which the average value of stellar volume emissivity is higher than zero can be treated approximately as a discrete radiation source. In the following, we will refer to this kind of cell as an ‘emitting cell’. Similarly, cells with average dust density higher than zero will be referred to as ‘dusty cells’.

⁴ For example, the latter condition for a single grain stochastically heated can be expressed as

$$\int Q_{\lambda, \text{abs}} \int B_\lambda(T) P(T) dT d\lambda = (c/4\pi) \int Q_{\lambda, \text{abs}} U_\lambda d\lambda,$$

where $Q_{\lambda, \text{abs}}$ is the grain absorption efficiency at wavelength λ , $B_\lambda(T)$ is the Planck function calculated for dust temperature T and $P(T)$ is the probability for the dust grain to have a temperature equal to T . Numerical methods, such as the one presented in Guhathakurta & Draine (1989), allow us to derive $P(T)$ and therefore the dust emission spectra, once the absorption efficiency $Q_{\lambda, \text{abs}}$ and the RFED U_λ are known.

Then, one performs ray tracing for a large set of directions originating from the centres of the emitting cells. That is, one follows the variation of the specific intensity $I_\lambda(\mathbf{x}, \mathbf{n})$ from the cell centres along rays corresponding to each direction \mathbf{n} . While following a ray, one considers the increase of radiation intensity $I_\lambda(\mathbf{x}, \mathbf{n})$ due to the stellar volume emissivity in the cell originating the ray but not in the intersected cells, where only the decrease of intensity due to dust absorption and scattering is considered. This allows us to calculate separately the contributions δU_λ provided only by the emitting cell originating the ray to the final value of $U_\lambda(\mathbf{x})$ in all the cells intersected by the same ray.⁵ When a ray intersects a cell i different from the original cell, the new value of the specific intensity will then be

$$I_{\lambda, i+1} = I_{\lambda, i} e^{-k\rho_c \Delta r}, \quad (3)$$

where ρ_c is the cell dust density and Δr is the *crossing path*. For each ray–cell intersection one calculates an appropriate average of the value of I_λ within the ray crossing path and, thus, the contribution δU_λ to the local value of $U_\lambda(\mathbf{x})$ by using a discrete version of equation (2). When all the rays from one emitting cell have been processed, the ray tracing is performed from another emitting cell and so on until all the emitting cells have been considered. Scattered radiation, whose intensity in a finite number of directions has also been stored locally for each ray–cell intersection, is then processed in a similar fashion.

If one creates a grid sufficiently fine in resolution and launches a sufficiently large number of rays, the calculated cell RFED values are very close to the exact values of $U_\lambda(\mathbf{x})$ at the cell centres and can be used to calculate the dust heating. Furthermore, the described procedure is extremely flexible and capable to handle completely arbitrary 3D distributions of stellar luminosity and dust mass. Unfortunately, the implementation of the procedure in the simple form described above is too computationally expensive (scaling approximately as $N^{5/3}$, with N being the total number of cells, in the case of uniform spatial sampling), considering also that the calculation has to be performed in an iterative way for the scattered light and for different wavelengths. Nonetheless, for well-mixed emitters–absorbers geometries, such as in the case of galaxy dust–stellar distributions, the full ray-tracing calculation for rays propagating throughout the entire model from each emitting cell does not have to be necessarily performed to obtain a reasonably accurate solution for $U_\lambda(\mathbf{x})$.

In fact, each radiation source in a general RT problem not necessarily contributes significantly to U_λ at each position within the volume considered for the RT calculation but often only within a fraction of it, which we call the ‘source influence volume’. In the ray-tracing method described above, if one knew in advance the extent of the influence volume for each emitting cell, it would be possible to reduce the number of calculations by simply performing ray-tracing only within this volume. Unfortunately, it is not possible to know this information a priori, since the final values of U_λ at each position are available only *after* performing the RT calculation. However, one can estimate in a conservative way the extent of the influence volume for a given emitting cell. The basic idea is to identify a point at some distance from the emitting cell where it can be proved that the contribution δU_λ carried by a ray is negligible

⁵ This approach can be redundant because the rays originating from different cells can often go through almost the same paths. On the other side, it is convenient because it easily allows the implementation of the acceleration techniques presented in this work.

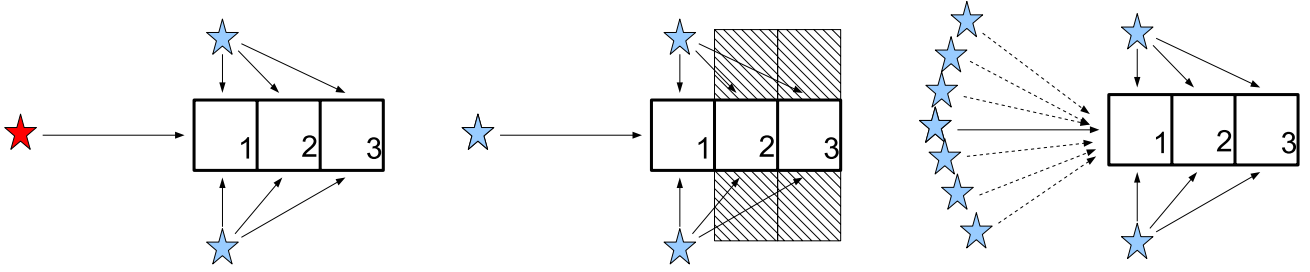


Figure 1. Examples of stars and dust geometries where the criteria to identify the limit of a source influence volume works (left-hand panel) or can fail (middle and right-hand panel). Left: the ray coming from the distant source does not contribute significantly to the RFED in cell 1, which is illuminated mainly by other sources. As a consequence, the same ray does not contribute significantly also to the cells beyond cell 1. Middle: as in the left-hand panel, the ray from the distant source does not contribute significantly to the RFED in cell 1. However, in this particular geometry, its contribution to the RFED in the cells beyond cell 1 cannot be negligible because the emission from the other sources is highly attenuated by dust (dashed cells). Right: the distance source is part of a large emitter distribution, whose individual RFED contributions to cell 1 are very small but the cumulative contribution cannot be negligible.

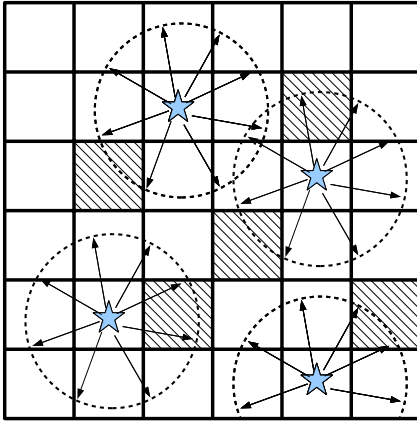


Figure 2. First estimate of the RFED. The radial ray tracing is performed only until a limit optical depth or distance. Dashed squares denote cell containing dust.

compared to the local final value of U_λ . If this is the case, this can imply that the emitting cell will not contribute significantly to U_λ beyond that position, which is already outside the influence volume of the emitting cell [see Fig. 1 for simple examples where this criteria will work (left-hand panel) or can fail (middle and right-hand panels) if not properly applied].

In practice, one can implement this method in the following way. First, one calculates a lower limit $U_{\lambda,LL}$ for U_λ within the entire volume by performing ray tracing from each emitting cell only until a certain arbitrary distance (see Fig. 2). Once the lower limit for U_λ is calculated, one can start the RT calculation again from the beginning but this time is able to check if a contribution δU_λ , carried by a ray to a particular cell, is going to be significant or not. In fact, if for a certain intersected cell δU_λ is negligible compared to the local value of the lower limit $U_{\lambda,LL}$, then it will be negligible also compared to the final value of U_λ at that position. The actual implementation of this method consists in checking at each cell intersection if $\delta U_\lambda < f_U \times U_{\lambda,LL}$ with f_U equal to a very small number to be chosen appropriately (see Section 4 for discussion on this point). When this condition is realized and if the chosen value of f_U is sufficiently small, then the contributions δU_λ will also be negligible for all the cells beyond that position in the same ray direction.

This implies that, once $\delta U_\lambda < f_U \times U_{\lambda,LL}$ at a certain distance from an emitting cell along a ray path, one can stop the ray-tracing calculation for that particular ray at that position. In fact, in that

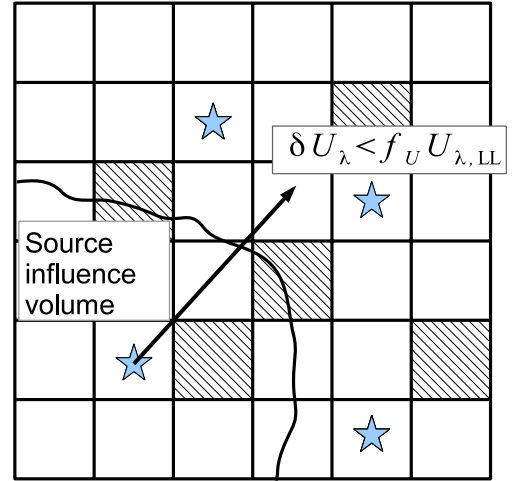


Figure 3. Ray-tracing calculation from one source until $\delta U_\lambda < f_U \times U_{\lambda,LL}$. The position when this condition is realized should be outside the source influence volume. Thus, one can stop the ray-tracing calculation at that position.

case, the intersected cell is already outside the influence volume of the emitting cell originating the ray (see Fig. 3). In this way, the total amount of calculations to be performed can be substantially reduced, making it feasible to use a modified version of the above ray-tracing algorithm to infer the U_λ distribution within complex dust/stars structures as those observed in galaxies. In the following subsection, we provide a simplified description of the RT algorithm we have developed based on this approach.

2.2 Basic description of the DART-RAY algorithm

In the following we provide a simple description of the three steps performed by the algorithm which implements the solution strategy outlined above to calculate the RFED distribution U_λ at a single wavelength λ . This description assumes that a grid of cells subdividing the entire model has already been created. A complete technical description of the code will be given in Section 3.

First step: calculation of a lower limit for U_λ . The first step consists of ray-tracing from each emitting cell adopting a ray angular density such that *all* the cells within a certain radius or a certain optical depth from each emitting cell are intersected by multiple rays, as shown in Fig. 2 (hereafter, we will refer to the process of intersecting all cells in a certain region with multiple rays as ‘fully

sampling' that region). The specific values for the limit radius and optical depth can be specified in the input. They should be large enough to let the rays cover a relatively large fraction of the entire model but small enough to avoid a too long computational time in this step. The inferred contributions δU_λ to the value of U_λ in each cell crossed by rays are accumulated into an array $U_{\lambda,LL}$ (LL stays as 'lower limit'). As said before, the inferred RFED distribution $U_{\lambda,LL}$ represents only a lower limit for the final value U_λ since there could be other emitting cells, at distances larger than those adopted limits, whose contribution to U_λ at each particular point has not been considered yet. In addition, scattered light contributions have also been neglected at this point.

Second step: processing of source direct light. In the second step the ray-tracing procedure is repeated again from the beginning but this time the rays fully sample the regions around each emitting cell, until the ray contribution δU_λ for an intersected cell become smaller than a very small fraction of the lower limit $U_{\lambda,LL}$, that is until $\delta U_\lambda < f_U \times U_{\lambda,LL}$ with f_U being a very small number (see Section 4 for more details about how to choose an appropriate value for f_U). When this condition is realized, it means that the position reached by the ray is outside the emitting cell influence volume (see Fig. 3) and the final value of U_λ in the crossed cell is contributed mainly by emitting cells different from the emitting cell originating the ray.⁶ Therefore, to the purpose of calculating the RFED distribution U_λ , there is no reason to proceed with a full sampling of the cells beyond the limit determined in this way. Apart from storing the values of the RFED contributions δU_λ , after each ray crosses a cell, the scattered energy information are also stored for that cell. That is, the luminosity scattered within a discrete set of solid angles is stored for each cell containing dust. These values will be used in the next step. Before going to the third step, the value of $U_{\lambda,LL}$ is updated with the current estimation for U_λ .

Third step: scattering iterations. After the direct light has been processed in the second step, a third step is started where there is a series of iterations to process the scattered radiation. Each cell which originates scattered light is treated as an emitting cell exactly in the same way as in step 2. Ray tracing is performed from each dusty cell by fully sampling all the volume surrounding the cell until the contribution δU_λ is negligible compared to a small fraction of $U_{\lambda,LL}$, the lower limit for U_λ updated with the new value of U_λ found in step 2. Again, scattering information is stored as well after each ray crossing and this higher order scattered radiation intensity is processed in successive iterations. These scattering iterations continue until the vast majority of the luminosity of the system has been either absorbed by dust or has escaped outside the model. That is, until $\Delta L_\lambda < f_L L_\lambda$, where L_λ is the total stellar luminosity emitted within the model, ΔL_λ is the amount of luminosity still to be processed (that is, not absorbed or escaped yet) and f_L is a parameter to be set in the input.

⁶ Note that, as shown in the right-hand panel of Fig. 1, there could be emitting cells which are part of a large emitting cell distribution, whose individual RFED contributions δU_λ might be lower than the assumed energy density threshold $f_U U_{\lambda,LL}$, but the cumulative contribution is not negligible. Overlooking the presence of this kind of cells can be avoided by choosing an appropriate value for the constant f_U . However, in cases such as that of an extended distribution of uniform volume emissivity within an optically thin system, the value of f_U to be chosen, in order to reach an accurate solution, could be extremely low. In those cases, there might be no substantial advantage in terms of speed by using the presented algorithm, since the majority of emitting cells contribute significantly to the RFED at each position in the entire volume.

The disadvantage of this procedure is that many of the calculations performed in the first step are repeated once again in the second step. The advantage is that the number of calculations avoided can be very high, thus reducing significantly the total calculation time for those geometries where the influence volumes of the emitting cells are only a small fraction of the total volume. Further characteristics of the code, not mentioned in the simplified algorithm above, include the adaptive and directional-dependent angular density of the rays (see Section 3.2) and the methods implemented to calculate the specific intensity of the radiation escaping outside the model in a finite set of directions (see Section 3.4).

3 THE RAY-TRACING 3D CODE: TECHNICAL DESCRIPTION

In this section we provide an extensive description of the code we have developed. The code consists of two main programs performing the adaptive grid creation and the RT calculation, respectively. In the following subsections, we describe the adaptive grid creation (Section 3.1), the basic ray-tracing routine (Section 3.2) and each of the three steps of the RT algorithm in detail (Section 3.3). Finally, we describe the methods implemented to derive the escaping radiation specific intensity (Section 3.4).

3.1 Adaptive grid creation

Given an input spatial distribution of dust mass and stellar luminosity (either defined by analytical formulae or in a tabulated form), an adaptive grid is created in a way such that the spatial resolution is higher in regions where the radiation field intensity is expected to vary in a more rapid way, such as those where the density of dust is higher. A parent cell of cubic shape, enclosing the entire model, is subdivided in $3 \times 3 \times 3 = 27$ child cubic cells of equal size.⁷ Then, the average dust density and stellar volume emissivity are calculated within the volume of each newly created cell, together with an estimation of their variation within each cell. Further cell subdivision proceeds for those child cells which do not satisfy user-defined criteria and those cells become parents of even smaller child cells. After that, the estimation of the cell dust density/stellar volume emissivity and the cell subdivision procedure are performed for the new cells and so on. In this way, a tree of cells is constructed iteratively until the chosen criteria are satisfied for all the smallest cells within each original parent cell. Also, in order to obtain a smooth variation of the grid resolution, further cell subdivision is performed to avoid differences in cell subdivision level higher than one between neighbour cells. The cells which have not been further subdivided, after the entire grid creation has been completed, are called the leaf cells.

The criteria for cell subdivision should be chosen in order to obtain both numerical accuracy and an adequate coverage of the RFED distribution within the model. In order to achieve a good numerical accuracy, it is important to have leaf cells with small total optical depths and with small gradients of dust density and stellar volume emissivity within the cells. For example, typical conditions for a cell to be a leaf cell could be

$$\tau_\lambda \ll 1 \quad (4)$$

⁷ We use a grid refinement factor equal to 3, since it has the advantage of preserving the position of cell centres after each cell subdivisions. For technical reasons, this facilitates the inclusion in the grid of central emitting point sources such as those in the solutions described in the next section.

$$\frac{\Delta\rho}{\rho_c} < 0.5, \quad (5)$$

where $\tau_\lambda = k_\lambda \rho_c l_c$ is the total cell optical depth, $\Delta\rho$ is an estimate of the dust density variation within a cell and ρ_c is the average cell dust density. An equivalent condition, as the one expressed by equation (5), has to be fulfilled by the cell stellar volume emissivity $j_{\lambda,c}$. These conditions allow us to use the simple expression given by equation (3) to calculate the variation of the specific intensity within a cell to a good degree of accuracy. However, note that an additional constraint is the maximum allowed number of subdivision levels NLVL_MAX, which has to be chosen in the input as well. The value of this parameter should be such to guarantee that the input cell parameter requirements, such as those above, are valid for all or at least the vast majority of cells in the model and, at the same time, avoid to create models with too many cells. It is desirable to keep the number of cells as low as possible, since it is one of the main parameters affecting the total computational time. After creating the grid, the program creates a table where the user can read the maximum and average cell parameters and, thus, quickly verify to which degree the input cell requirements have been fulfilled.

All the information which define the grid is printed on a file that can be read from the RT program. This includes:

- (i) – cell id number,
- (ii) – position of cell centre in Cartesian coordinates,
- (iii) – cell child number: which is equal to ‘-1’ if the cell is a leaf cell or to the id number of the first child cell created during the cell subdivision,
- (iv) – cell index number: binary code expressing the position of the cell within the cell tree,
- (v) – cell size l_c ,
- (vi) – cell dust density ρ_c and
- (vii) – cell stellar volume emissivity $j_{\lambda,c}$.

3.2 The basic ray-tracing routine

In this subsection we describe the basic ray-tracing calculation for rays departing from an emitting cell and propagating throughout the model. This is the core routine used by the RT algorithm described in the next subsection. Given an emitting cell, rays are casted into multiple directions defined by using the HEALPix sphere pixelation scheme (Górski et al. 2005, see also e.g. Bisbas et al. 2012; Abel & Wandelt 2002 for other applications in RT codes). In this scheme a sphere is divided in 12 main sectors of equal size, which can be further subdivided in smaller spherical pixels (see Fig. 4). By assuming that an HEALPix sphere is centred on the emitting cell centre, the lines connecting the cell centre to the centre of the HEALPix spherical pixels define directions along which one can follow the variation of the specific intensity within the model. The use of the HEALPix routines PIX2ANG_NEST (translating pixel index numbers into spherical coordinates) and its inverse ANG2PIX_NEST is a convenient way to handle sets of rays with an adaptive angular density (see below).

For each ray, the following approximations are implemented:

- (1) the calculation is performed as if all the cell luminosity propagates through solid angles defined by the pixels of an HEALPix sphere centred on the cell centre;
- (2) since one can only follow the exact variation of I_λ along the finite set of HEALPix directions, it is assumed that the evolution of I_λ along all the directions included within the total solid angle associated with a ray (determined by the adopted HEALPix scheme

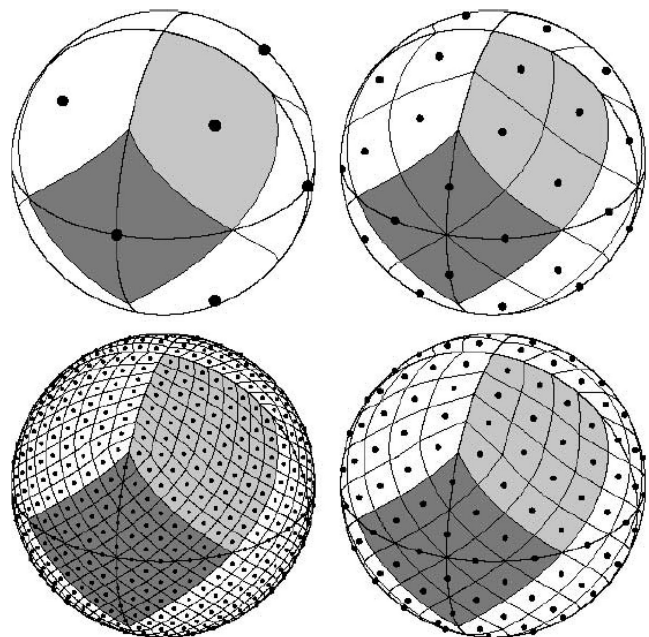


Figure 4. Healpix sphere at different angular resolution. The spherical pixels in the upper-left sphere are those mentioned as ‘HEALPix main sectors’ in the text. Figure from Górski et al. (2005) (reproduced by permission of the AAS).

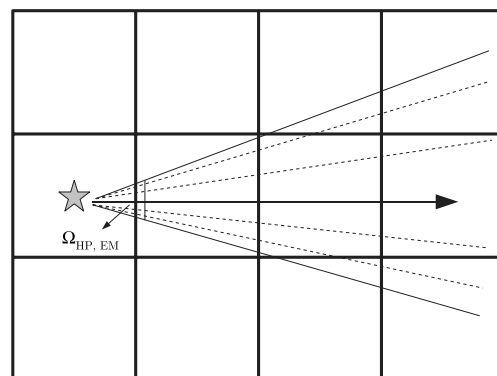


Figure 5. Ray beam associated with an HEALPix pixel, propagating throughout the model. During the RT calculation, the variation of I_λ is followed only along the main direction (bold arrow). The same variation is assumed for the other directions within the same ray beam (dashed lines). Note that at large distances from emitting cell, the beam begins intersecting more cells simultaneously.

angular resolution) is exactly the same as for the main central ray direction (see Fig. 5).

The above approximations imply that the total luminosity density associated with a ray and flowing through an HEALPix solid angle $\Omega_{\text{HP,EM}}$ at any distance r from the centre of the emitting cell is given by

$$L_{\lambda,\text{ray}}(r) = I_\lambda(r) \Omega_{\text{HP,EM}} A_{\text{EM}}, \quad (6)$$

where A_{EM} is the projected area of the emitting cell (assumed to be equal to the emitting cell size squared).

The variation of I_λ , when the associated ray crosses a cell, is calculated using the following expressions. The variation due to the

crossed optical depth $\tau_\lambda = k_\lambda \rho_c \Delta r$ and cell volume emissivity $j_{\lambda,c}$ within the cell originating the ray is equal to

$$I_{\lambda,0} = \frac{j_{\lambda,c} \Delta r}{\tau_\lambda} (1 - e^{-\tau_\lambda}) \quad (7)$$

if $\tau_\lambda > 0$ (cell containing dust).⁸ If $\tau_\lambda = 0$, we assumed

$$I_{\lambda,0} = j_{\lambda,c} \Delta r, \quad (8)$$

which is consistent with the previous expression when $\tau_\lambda \rightarrow 0$. During the scattering iterations, the scattered light is considered for the calculation of the cell volume emissivity, as it will be shown later. Instead, the new value of I_λ after the crossing of a ray through a cell different from the original one is simply given by

$$I_{\lambda,i+1} = I_{\lambda,i} e^{-\tau_\lambda}. \quad (9)$$

Apart from calculating a new value for I_λ , when a ray crosses a cell, the code determines the contribution of the ray to the intersected cell RFED and the amount of energy scattered by the dust in the intersected cell. However, these contributions can be accurately calculated only if a sufficiently high ray angular density is used. In fact, depending on the cell sizes and the adopted HEALPix angular resolution, at any distance from the emitting cell, the ray beam as a whole (not just the main ray direction) can intersect either a single cell or a group of cells at the same time. At distances large enough from the emitting cell, the beam, originally intersecting only one cell at a time, will begin intersecting more cells simultaneously (see Fig. 5). As said before, the code traces the evolution of I_λ only along the main direction of the ray beam and it is assumed that for all the directions within the beam the I_λ variation is exactly the same. However, far away from the emitting cell, the beam propagates through larger physical volumes and the previous approximation can become very inaccurate. Actually, in order to obtain a precise calculation of the RFED contributed by an emitting cell C_{EM} to a certain cell C_{INT} , it is desirable that several rays originating from C_{EM} are intersecting C_{INT} . In this way, the calculation of RFED is more accurate because of the better estimation of the average I_λ within the intersected cell.

If one defines A_{INT} , the projected area of the intersected cell (approximated by the cell size squared), and $\Omega_{INT} = \frac{A_{INT}}{r^2}$, the solid angle subtended by the projected area of the intersected cell and with origin in the centre of the emitting cell (see Fig. 6), in order to have more rays from C_{EM} crossing C_{INT} one requires that

$$\Omega_{HP,EM} < \frac{\Omega_{INT}}{N_{rays}}, \quad (10)$$

where N_{rays} is an input parameter equal to the minimum number of rays which should cross C_{INT} . If this condition is fulfilled by all the intersected cells within a certain region around an emitting cell, we say that the rays are ‘fully sampling’ that region, using the same terminology already introduced in Section 2.2.

Once the above condition is fulfilled for an intersected cell, the code defines $\Omega = \Omega_{HP,EM}$ and the contribution of a ray to the intersected cell RFED $\delta U_{\lambda,INT}$ is given by

$$\delta U_{\lambda,INT} = \frac{\langle I_\lambda \rangle A_{EM} \Omega \frac{\Delta r}{c}}{V_{INT}}, \quad (11)$$

where c is the speed of light, $\frac{\Delta r}{c}$ is equal to the time needed by the light to cross the intersected cell, V_{INT} is the volume of the

⁸ Actually the numerical implementation requires to assume a small threshold value higher than zero, such that $e^{-\tau_\lambda} \neq 1$ when the exponential function is evaluated.

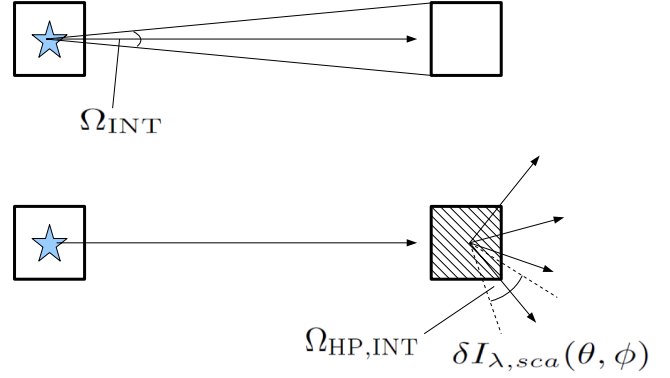


Figure 6. Definitions of the solid angle subtended by an intersected cell Ω_{INT} , the scattered intensity $I_{\lambda,sca}(\theta, \phi)$ from an intersected cell and the intersected cell HEALPix solid angle $\Omega_{HP,INT}$.

intersected cell and the average value of I_λ along the crossing path is equal to

$$\langle I_\lambda \rangle = \frac{I_{\lambda,i} (1 - e^{-\tau_\lambda})}{\tau_\lambda}, \quad (12)$$

if $\tau_\lambda > 0$ and

$$\langle I_\lambda \rangle = I_{\lambda,i} \quad (13)$$

if $\tau_\lambda = 0$.

The ray contribution to the specific intensity scattered by the intersected cell $\delta I_{\lambda,sca}(\theta, \phi)$ is (see Fig. 6)

$$\delta I_{\lambda,sca}(\theta, \phi) = \frac{I_{\lambda,ext} w_{\lambda,sca} A_{EM} \Omega \Phi(\theta, \phi)}{A_{INT} \Omega_{HP,INT}}, \quad (14)$$

where $w_\lambda = \frac{k_{\lambda,sca}}{k_{\lambda,ext}}$, $\Omega_{HP,INT}$ is the solid angle determined by the HEALPix angular resolution adopted to store the scattered radiation intensity in the intersected cell, $\Phi_{HG}(\theta, \phi)$ is a term representing the integration of the Henyey–Greenstein scattering phase function over the solid angle $\Omega_{HP,INT}$:

$$\Phi_{HG}(\theta, \phi) = \frac{\Omega_{HP,INT}}{4\pi} \frac{1 - g_\lambda^2}{[1 + g_\lambda^2 - 2g_\lambda \cos(\theta)]^{3/2}} \quad (15)$$

and $I_{\lambda,ext}$ is the amount of ray specific intensity absorbed or scattered by the cell, which is given by

$$I_{\lambda,ext} = I_{\lambda,i} (1 - e^{-\tau_\lambda}). \quad (16)$$

The scattered luminosity values (numerator of equation 14) are accumulated for each cell on an array $SCATT_EN(\theta, \phi)$ for a certain set of HEALPix directions, whose angular density can be specified in the input according to memory availability.⁹ Of course, a higher numerical accuracy will be achieved if the scattered intensity values are stored with a higher angular resolution.

In case the condition expressed by equation (10) is not fulfilled, all the equations above are still used but with $\Omega = \Omega_{HP,EM}$ if $\Omega_{HP,EM} < \Omega_{INT}$ and $\Omega = \Omega_{INT}$ if $\Omega_{HP,EM} > \Omega_{INT}$. That is, we consider only the beam luminosity passing through the intersected cell. As it will be explained later, condition 10 is not required to be fulfilled beyond the regions where full sampling is desired. That means, beyond a certain distance from an emitting cell there could be cells which are not intersected by any ray and therefore none of the above quantities is calculated by the code for those cells.

⁹ The $SCATT_EN$ array can be very large: dimension = number of cells $\times 4\pi/\Omega_{HP,INT}$.

The formulae given above are different when the crossed cell coincides with the emitting cell originating the rays. In this case one has also to take into account the internal volume emissivity of the cell. Therefore, the average value of I_λ needed to calculate the ray contribution to the local RFED by using equation 11 is given by

$$\langle I_\lambda \rangle = \frac{j_{\lambda,c} \Delta r}{\tau_\lambda^2} (e^{-\tau_\lambda} - \tau_\lambda - 1), \quad (17)$$

if $\tau_\lambda > 0$ and

$$\langle I_\lambda \rangle = \frac{j_{\lambda,c} \Delta r}{2}, \quad (18)$$

if $\tau_\lambda = 0$. Instead the value of $I_{\lambda,\text{ext}}$ in equation (14) is given by

$$I_{\lambda,\text{ext}} = \frac{j_{\lambda,c} \Delta r (e^{-\tau_\lambda} + \tau_\lambda - 1)}{\tau_\lambda} \quad (19)$$

and all the quantities with subscript INT in equations (11) and (14) refer to the emitting cell in this case. During scattering iterations, the term $j_{\lambda,c} \Delta r$ in the previous equations is substituted by $I_{\lambda,\text{sca}}(\theta, \phi)$, the specific intensity of the total scattered radiation accumulated locally on each cell (see equation 14).

3.3 The radiative transfer algorithm

3.3.1 Step 1: calculation of a lower limit for the RFED

In the first step of the RT algorithm, ray tracing is performed from each emitting cell by fully sampling all the cells until the rays cross a limit optical depth or distance specified in the input (see Fig. 2). In this way the contributions from each emitting cell to the RFED in the areas around those cells are summed up to obtain a lower limit $U_{\lambda,\text{LL}}$ for the RFED distribution in the entire model. Full sampling of a region of cells centred on an emitting cell requires a sufficient amount of rays to be launched from the emitting cell. However, the ray angular density necessary to achieve full sampling can vary depending on the angular direction. In order to optimize the number of rays, our code has the additional peculiarity that the angular distribution of rays originating from emitting cells is not homogeneous. Specifically, the ray angular density is optimized within an initial HEALPix sector by the following iterative procedure (see flow diagram in Fig. 7).

A first ray-tracing attempt is performed with an initial HEALPix angular resolution, e.g. the calculation is performed only for the direction passing by the centre of an HEALpix main sector.¹⁰ The beam defined by the chosen HEALPix pixel will intersect the cells progressively more distant from the emitting cell. As said in the previous subsection, in order to have an accurate estimation of the radiation field contribution δU_λ carried by the beam to an intersected cell, it is necessary that the entire beam is passing through the cell, together with at least several other adjacent beams. Therefore, when an intersected cell is found, the code checks if the condition expressed by equation (10) is fulfilled. When this happens, the contribution to the RFED is stored in a temporary array U_{TEMP} and the ray tracing continues to the next intersected cell in the same way. When the above condition is not realized, the U_{TEMP} array is initialized and the radial ray tracing re-starts from the beginning but with a higher HEALpix angular resolution. That is, more rays are launched within the initial HEALpix sector. In this way, smaller beams are generated until condition (10) is always fulfilled for all

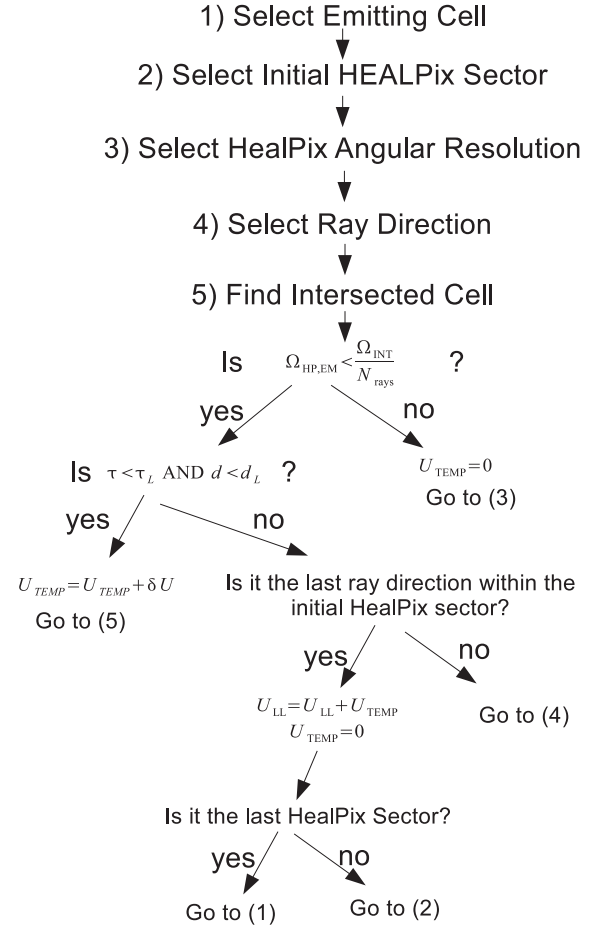


Figure 7. Flow diagram of the procedure used to estimate the lower limit of the RFED.

the intersected cells within the input-defined distance or optical depth crossed by each ray. When this is realized, the ray tracing can be performed without interruptions for all the rays within the chosen initial HEALPix sector. After the last ray within the initial HEALPix sector has been processed, the values of RFED stored in U_{TEMP} are added to the array U_{LL} and then U_{TEMP} is initialized. This iterative procedure is performed for all the initial HEALpix sectors, covering the entire sphere, and for each emitting cell.

3.3.2 Step 2: processing direct radiation

In the second step, the ray tracing is started from the beginning again following the same iterative procedure explained in the previous subsection but with some differences (see flow diagram in Fig. 8). As before, the angular density of the rays is increased until the intersected cells, where the contribution to the local RFED needs to be accurately calculated, are crossed by multiple rays. However, during this step the increasing of ray angular density is stopped if the contribution by a ray to an intersected cell RFED is a very small fraction of the value stored at that position in $U_{\lambda,\text{LL}}$. That is, when

$$\delta U_\lambda < f_U \times U_{\lambda,\text{LL}} \quad (20)$$

with f_U defined in the input (see Section 4). When this condition is fulfilled, it means that the emitting cell, originating the ray, is not contributing substantially to the RFED of the intersected cell under consideration and to all the other cells beyond that in the direction

¹⁰ See upper-left panel of Fig. 4 for definition of ‘HEALPix main sector.’

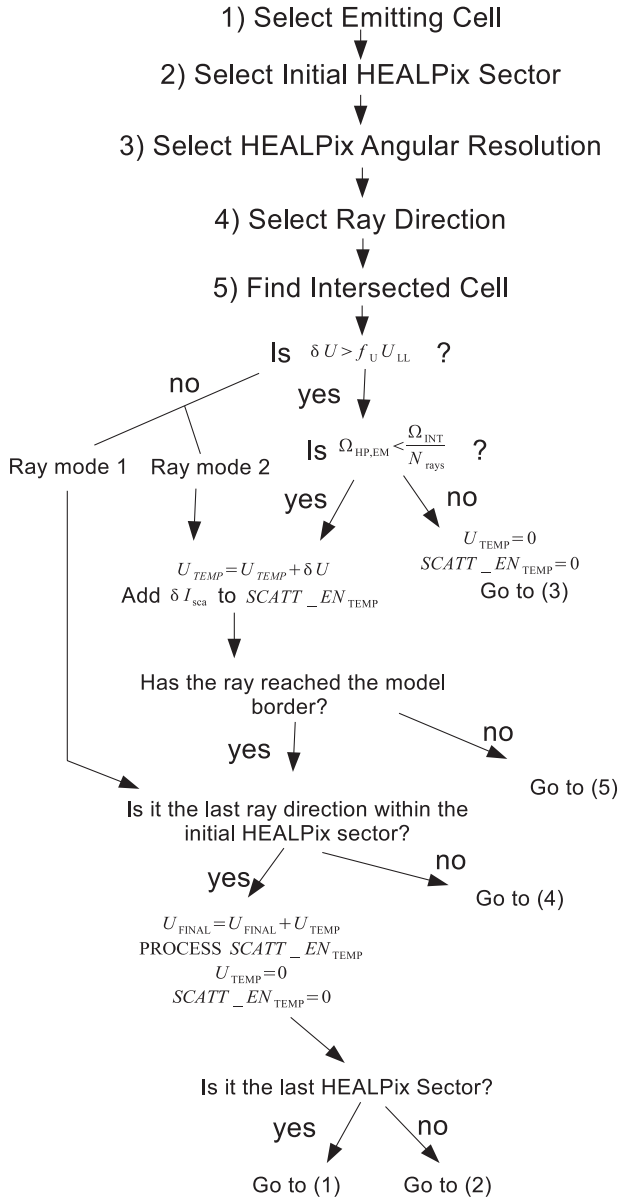


Figure 8. Flow diagram of the main RT procedure (used for processing both the direct and scattered light).

of the ray. In addition, at variance with step one, ray tracing is not necessarily limited in the region where full sampling is required, but optionally rays can keep propagating until the model border (this option will be referred to as ‘ray mode 2’). Similarly as before, the values of the RFED contributions are first stored in U_{TEMP} and then added to the array $U_{\lambda,FINAL}$, after the ray tracing from all the directions within the initial HEALPix sector is completed. After this procedure has been performed for all the emitting cells, $U_{\lambda,FINAL}$ contains all the contributions from direct radiation but still lacks the contribution from scattered light, which will be calculated in the next step. However, during this step, the scattered radiation energy information is stored after each cell crossing in the array $SCATT_EN(\theta, \phi)$. As explained in Section 3.2, this array contains the scattered radiation luminosity in a finite number of HEALPix beams, whose angular density is defined by the user according to memory availability. When a ray crosses a cell, the fraction

of scattered luminosity is angularly distributed according to the Henyey–Greenstein phase function (see equation 15).

3.3.3 Step 3: processing scattered radiation

The last step consists of the processing of the scattered radiation. Since the scattered radiation itself can be scattered multiple times, this step requires several iterations. However, the procedure for the ray tracing is completely the same as the one in the previous step once the scattered luminosity values, stored in the $SCATT_EN$ array, are considered to calculate the volume emissivity from each cell. The only difference is that, while in the previous steps the emission from each cell was isotropic, in this step the ray luminosities can depend on the angular direction. The $SCATT_EN$ values from each cell are on turn processed and initialized. Using the same optimization procedure described above, ray tracing from each cell is performed to calculate the contribution to $U_{\lambda,FINAL}$ and to the $SCATT_EN$ arrays of the intersected cells. After all the emitting cells have been processed once, a check on the remaining luminosity ΔL_{λ} stored in the $SCATT_EN$ array is performed. If this luminosity is higher than a very small fraction f_L of the total luminosity L_{λ} emitted by the entire model, that is, when $\Delta L_{\lambda} > f_L L_{\lambda}$, a new scattering iteration is started. If not, scattering iterations are stopped and the output of the entire calculation is printed on a file. The output includes both the RFED distribution and the escaping radiation specific intensity in several directions, calculated as described in the next section.

3.4 Calculations of the escaping radiation specific intensity

Although the algorithm we developed is optimized for the calculation of RFED distributions, our code can be used to derive the specific intensity of the radiation emitted or scattered by each cell and escaping outside the model volume. The code can calculate either averages for the radiation propagating within large solid angles or the specific intensity for the radiation propagating into single directions defined in the input. As it has been shown before, our code optimizes the angular density of the rays departing by each emitting cell in order to obtain a full sampling of cells where the ray RFED contribution is important. Beyond the region fully sampled, if specified in the input (so-called ray mode 2), rays can keep propagating throughout the model until the model border (although they can miss a progressively higher fraction of cells). When a ray arrives to the model border, it is possible to calculate the specific intensity of the escaping radiation, generated by the emitting cell in the ray direction:

$$I_{\lambda,esc} = I_{\lambda,o} e^{-\tau_{\lambda}}, \quad (21)$$

where τ_{λ} is the total optical depth crossed by the ray from the emitting cell to the model border. The calculation of $I_{\lambda,esc}$ can be done for all the rays belonging to the sets of rays within an HEALPix main sector, within which the ray angular density has been optimized as described in Section 3.3. It is then straightforward to calculate the following average:

$$\langle I_{\lambda,esc} \rangle = \frac{\sum I_{\lambda,esc,i} \Omega_{HP,EM,i}}{\Omega_{HP,MS}} \quad (22)$$

where $\Omega_{HP,MS} = 4\pi/12$ is the solid angle of an HEALPix main sector and the sum is performed for all rays passing within that solid angle. The average value $\langle I_{\lambda,esc} \rangle$ derived in this way can be used to measure the escaping luminosity within a HEALPix main sector

using equation 6 with $I_\lambda(r) = \langle I_{\lambda,esc} \rangle$. Note that this estimate assumes that the missed cells in the volumes beyond the fully sampled region have attenuation properties similar to those of the intersected cells at the same distance from the emitting cell.

The estimate of the escaping luminosity within an entire beam is useful to calculate the total amount of stellar luminosity escaping from the system. However, one would also like to store the escaping radiation specific intensity in a set of directions, which is what it would actually be observed on astronomical maps. To do this, we store the values of escaping radiation specific intensity from each cell, calculated using formula (21), for a user defined set of directions. Since far away from the model the rays reaching the observer are all parallel, one can consider the escaping radiation specific intensity coming from each emitting cell along parallel directions in order to create visual maps of the model as seen from different view angles (see an example in Fig. 26).

4 NOTES ON APPROXIMATIONS, IMPLEMENTATION AND PERFORMANCE

3D dust RT requires extremely high computational resources if one wants to obtain numerically accurate solutions for systems where both radiation sources and dust are distributed over different spatial scales. Practically, this implies that 3D dust RT codes need to be developed trying to balance the need for numerical accuracy with approximations reducing the total computational time to acceptable amounts.

While implementing the algorithm described in the previous section, we made use of the following approximations:

(1) the dust density value is assumed to be constant within each cell and, thus, within each cell crossing path. This allows us to use the simple exponential expression given by equation (3) to calculate the new value of the specific intensity of a ray after a cell crossing. However, the accuracy of the results is then affected by the spatial resolution of the grid. A more precise method would consist in using adaptive steps along a ray and calculating new values for the dust density at each position within the crossing path (see e.g. Steinacker et al. 2003). However, these extra calculations would increase substantially the total calculation time.

(2) The angular sampling of scattered light in each cell is performed using a finite number of solid angles covering the entire sphere (see Section 3 for more details). That is, the contribution to the scattered light, calculated after a cell intersection, is stored in a number of directions corresponding to the dimension of the local SCATT_EN array, defined in Section 3 (typically 48 or 96 directions are used in the calculation presented below). This means, that some of the information on the angular distribution of the scattered light is neglected because of the relatively coarse sampling on the sphere.

(3) The increase of angular density for the rays departing from each emitting cell is stopped when the condition expressed by equation (20) for the ray contribution to the local RFED is realized. This is one of the characteristic features of our RT algorithm and probably the main one which allows us to reduce substantially the computational time. As mentioned in Sections 3.3 and 3.4, the code we developed gives the possibility of either simply stopping the rays at the locations where the above condition is realized (ray mode 1) or only avoiding the further increase of ray angular density beyond those points but still continuing the ray tracing until the model border (ray mode 2). In both cases, a fraction of the luminosity carried by the beam associated with the rays is not considered in the

calculation of the RFED distribution. Controlling the actual amount of this ‘lost luminosity’, not processed during the RT calculation, is fundamental to assure that approximate global energy balance is reached between the luminosity emitted by the stars and the sum of the luminosities absorbed and escaping from the system. In order to check this, we set up a counter of ‘lost luminosity’ which sum up the ray luminosity which is not processed during the calculation. Contributions to this sum are provided by the entire beam luminosity at the locations where condition (20) is realized. The input parameters directly affecting the amount of ‘lost luminosity’ are f_U and N_{rays} , which have to be chosen carefully such to guarantee energy balance. Practically, one first finds an appropriate combination of f_U and N_{rays} for a typical model such to obtain a low fraction of ‘lost luminosity’ at the end of the calculation. After that, it is usually enough to use the same combination for these parameters for similar models and check that approximate energy balance has been achieved after each calculation. For all the calculations presented in the next section, we checked that, for the assumed combinations of those input parameters, the total lost luminosity is always less than 1 to 2 per cent of the total stellar luminosity.

The algorithm has been implemented in a Fortran 90 code, which is a typical language used in high-performance computing (HPC). Parallelization of the code has been implemented using the application programming interface OpenMP, which allows parallel computing on shared-memory machines. We opted for OpenMP parallelization since it required only a relatively small number of extra lines within the existing code. Furthermore, given the additive nature of the RT problem, it has been possible to develop simple programs to distribute the calculations for different sets of emitting cells among different nodes in a computer cluster. Within each node the calculation can be performed in parallel mode without the need of communication between nodes, except when arrays sums are needed at the end of each step of the RT algorithm or between scattering iterations. Extra routines have been written to perform these sums and this has been sufficient to perform RT calculations on computer clusters without the need of more elaborated message passing interface parallelization.

The test runs presented in the next subsection have been performed using the computing facilities at the University of Central Lancashire in Preston (in particular the local HPC cluster) and at the Max Planck Institute für Kernphysik in Heidelberg. The computational times and memory required vary depending on the geometry of the model, the spatial resolution adopted and the number of CPUs used. For example, a typical single wavelength calculation for a disc galaxy model (see Section 5.2) with a grid containing of the order of 10^5 cells can take about 2 d by using 64 CPUs with 2.57 GHz clock rate (and by using a f_U parameter low enough to achieve energy balance within less than a per cent). In terms of memory, this calculation requires few gigabytes of RAM memory (exact amount varies during the calculation because of the temporary ‘allocatable’ arrays vastly used by our code). The mentioned calculation time seems to be rather longer compared to that needed by MC codes where acceleration techniques are well developed and which are able to handle multiwavelength photon packages simultaneously (see e.g. Jonsson 2006; Baes et al. 2011). However, one should notice that, at variance with ray-tracing codes, MC codes are not typically used to obtain accurate calculations of the monochromatic RFED distribution. Applications of MC methods focus on obtaining a good calculation for the escaping multiwavelength spectra. In order to predict the dust emission, this requires only the dust temperature in

each cell to converge and not necessarily each single value of the RFED at each wavelength.

5 COMPARISONS WITH OTHER CODES

In the following we describe and show the results of the comparisons with two codes: the 1D code `DUSTY` (Section 5.1) and the 2D code used in Popescu et al. (2011) (Section 5.2).

5.1 Comparison with `DUSTY` code

We performed a series of tests by comparing the results provided by our code with those obtained using the latest version of the RT code `DUSTY` (Ivezic & Elitzur 1997). Specifically, we considered the geometric configurations of the benchmark solutions of Ivezic et al. (1997, 197), with parameters equivalent or similar to those adopted in that paper. The `DUSTY` code can be used to solve the dust RT problem for a geometry consisting of a single central radiation source illuminating a spherically symmetric shell of dust with an arbitrary dust density radial profile. In this case, one can reduce the 3D RT equation to a 1D equation for the mean radiation field intensity by taking advantage of the spherical symmetry of this configuration. Furthermore, the `DUSTY` code utilizes several scaling properties of the RT problem. These are used to calculate sets of solutions which do not depend on the absolute values of the luminosity of the central source and of the dust density and opacity but only on their spatial variation or wavelength dependence. Thus, given a dust radial density profile in the shell and the wavelength dependence of the dust optical properties, this specific RT problem can be completely defined once the following parameters are specified:

- the effective temperature T_{source} of the central source, which we assumed emits as a blackbody;
- the dust temperature T_1 at the inner radius of the shell;
- the total radial optical depth τ ;
- the outer to inner radius ratio $Y = r_2/r_1$.

As in I97, we performed RT calculations for two types of radial profiles of the dust density distribution:

- (1) a constant density profile $\rho(r) = \rho_o$;
- (2) a power-law density profile $\rho(r) = \rho_o \left(\frac{r}{r_1}\right)^{-2}$,

for r in the range $[r_1, r_2]$ and $\rho(r) = 0$ for any other value of r .

The dust opacity coefficients per unit dust mass are defined as follows:

$$q_{\lambda, \text{abs}} = q_{\lambda, \text{sca}} = 1 \quad (23)$$

for $\lambda < 1 \mu\text{m}$ and

$$q_{\lambda, \text{abs}} = \frac{1}{\lambda}; \quad q_{\lambda, \text{sca}} = \frac{1}{\lambda^2} \quad (24)$$

for $\lambda > 1 \mu\text{m}$.

Scattering is considered isotropic in the `DUSTY` code, which corresponds to assuming $g_\lambda = 0$ in the scattering Henyey–Greenstein phase function used by our code.

For both forms of dust density profiles specified above, we performed two series of tests where we compared the results for the dust temperature radial profile and the outgoing radiation spectra. First, we created a grid of models by varying the inner radius dust temperature T_1 and keeping all the other parameters fixed to the same values. For a fixed amount of dust mass, a higher value of T_1 implies a higher dust luminosity which can be self-absorbed by

dust. Since self-absorption is not included in our code yet, at least some of the discrepancies evidenced by this test can be due to this effect. We will refer to this test in the following as ‘the dust temperature’ test. In a second series of tests, we have varied the value of τ while maintaining all the other parameters constant. By increasing the value of τ , the source luminosity is absorbed more efficiently and dust heating due to self-absorption could become progressively more dominant, especially at larger radii. We will refer to this test as ‘the optical depth’ test.

The specific parameters used in the ‘dust temperature’ test are the following: $Y = 1000$, $T_{\text{source}} = 2500$ K, optical depth at $1 \mu\text{m}$ $\tau_1 = 1$ and $T_1 = 200, 400, 800$ K. In the ‘optical depth’ test we used these parameters: $Y = 1000$, $T_{\text{source}} = 2500$ K, $\tau_1 = 2, 5, 10$ and $T_1 = 200$ K.

The first step performed by our code is the creation of a spatial grid sampling the entire model. To do this we require the absolute values of the central source luminosity and the physical distances corresponding to the inner and outer radius of the shell r_1 and r_2 , as these quantities are not explicitly specified in the input parameters of the `DUSTY` code. We derived these quantities from the standard output of the `DUSTY` code, which assumes that the bolometric central source luminosity is equal to $10^4 L_\odot$. Also, we obtained the absolute scaling of the dust density distribution ρ_o by using the following formulae:

$$\rho_o = \frac{\tau_1}{q_{1, \text{ext}}(R_2 - R_1)}, \quad (25)$$

for the case of the constant dust density radial profile and

$$\rho_o = \frac{\tau_1}{q_{1, \text{ext}} \frac{R_1}{R_2} (R_2 - R_1)}, \quad (26)$$

for the case of the power-law dust density radial profile. In the previous formulae $q_{1, \text{ext}} = q_{1, \text{abs}} + q_{1, \text{sca}}$ and the opacity coefficients are all evaluated at $1 \mu\text{m}$. We used the coefficients at this wavelength since they are the highest. This implies that the cell optical depths of the grid so created are the same or smaller at other wavelengths. For simplicity we used the same grid for all the wavelengths.

While creating the grid, we assigned average density values to each leaf cell containing dust. In the constant density profile case we simply assumed $\langle \rho_{\text{dust}}(r) \rangle = \rho_o$. In the power-law case, we used the following expression for the cell dust density, corresponding to the cell density average along a radial direction:

$$\langle \rho_{\text{dust}}(r) \rangle = \rho_o R_1^2 \left[\frac{1}{r_c - \Delta r/2} - \frac{1}{r_c + \Delta r/2} \right] / \Delta r, \quad (27)$$

where r_c is the radius corresponding to the cell centre and Δr is equal to the cell size. In the cases of the cells at the inner or outer border of the shell, we calculated averages by integrating the density only in the part of the cell containing dust and then dividing by the cell size.

We imposed the following conditions in the input of the grid creation program:

- (1) a cell has to be subdivided in smaller cells if the cell optical depth exceeds a small fraction of the total radial optical depth τ_1 , typically a factor of 0.01–0.03;
- (2) the minimum cell subdivision level is 3;
- (3) the maximum allowed cell subdivision level is equal to 7 and 8 for the constant and power-law dust density profile, respectively;
- (4) in the case of the power-law density profile, we also added the constraint that the maximum cell optical depth gradient is $\Delta \tau_{1 \mu\text{m}} / \tau_{1 \mu\text{m}} = 0.4$. These conditions have been chosen in order to achieve a solution with good numerical accuracy but also to

Table 2. 3D grid and input parameters for the ‘dust temperature’ test. Column (1) $p = 0$ refers to the constant dust density case and $p = 2$ to the power-law case. Columns (2) and (3) maximum and average cell optical depth at $1 \mu\text{m}$. Column (4) ray energy contribution threshold parameter. Column (5) minimum number of rays for cells within full sampling regions. Column (6) fraction of unprocessed total luminosity needed to end code iterations. Column (7) total number of cells. Note that the parameters do not depend on the specific value of $T_1 = 200, 400, 800 \text{ K}$. The total radial optical depth τ_1 is always equal to 1 for all the models.

| p | $\Delta\tau_{1,\text{max}}$ | $\langle\Delta\tau_1\rangle$ | f_U | N_{rays} | f_L | N_{cells} |
|-----|-----------------------------|------------------------------|--------|-------------------|-------|--------------------|
| 0 | 0.029 | 0.023 | 0.0001 | 16 | 0.001 | 302 481 |
| 2 | 0.23 | 0.006 | 0.001 | 16 | 0.001 | 214 326 |

Table 3. 3D grid and input parameters for the ‘optical depth’ test. Column (1) $p = 0$ refers to the constant dust density case and $p = 2$ to the power-law case. Column (2) total radial optical depth at $1 \mu\text{m}$. Columns (3) and (4) maximum and average cell optical depth at $1 \mu\text{m}$. Column (5) ray energy contribution threshold parameter. Column (6) minimum number of rays for cells within full sampling regions. Column (7) fraction of unprocessed total luminosity needed to end code iterations. Column (8) total number of cells. Note that the inner dust temperature is always $T_1 = 200 \text{ K}$ for all the models.

| p | τ_1 | $\Delta\tau_{1,\text{max}}$ | $\langle\Delta\tau_1\rangle$ | f_U | N_{rays} | f_L | N_{cells} |
|-----|----------|-----------------------------|------------------------------|--------|-------------------|-------|--------------------|
| 0 | 2 | 0.06 | 0.046 | 0.0001 | 16 | 0.001 | 302 481 |
| 0 | 5 | 0.15 | 0.11 | 0.001 | 4 | 0.001 | 302 481 |
| 0 | 10 | 0.29 | 0.23 | 0.001 | 4 | 0.001 | 302 481 |
| 2 | 2 | 0.45 | 0.013 | 0.001 | 16 | 0.001 | 214 326 |
| 2 | 5 | 1.13 | 0.032 | 0.001 | 16 | 0.001 | 214 326 |
| 2 | 10 | 2.2 | 0.064 | 0.001 | 16 | 0.001 | 214 326 |

avoid to create too many cells (that is, less than $\approx 10^6$ cells), thus reducing the amount of calculation time needed. In fact, note that the amount of cell subdivisions is limited by condition (3). Thus, in some parts of the model, a cell subdivision required by conditions (1) or (4) might not be performed because it would conflict with condition (3). The maximum and average values of the cell optical depths in each model are shown in Tables 2 and 3.

Once the grid has been created, before starting the RT calculation, one has to assign values to the following parameters (see Section 3): (1) f_U , the relative energy density contribution threshold above which a ray contribution to a crossed cell RFED is considered non-negligible; (2) N_{rays} , the minimum number of rays which has to cross a cell when the ray contributions are found not negligible; (3) f_L , the escaping luminosity threshold parameter, used to determine when the scattering iterations have to stop. The adopted values are also shown in Tables 2 and 3.

For each model, we performed the calculation at the following wavelengths: $0.443, 1.05, 1.1, 1.15, 1.2, 1.259, 1.3, 1.8, 2.2, 5.0, 10, 20 \mu\text{m}$. We calculated only one point for $\lambda < 1 \mu\text{m}$, that is at $\lambda = 0.443 \mu\text{m}$, because the opacity coefficients used by I97 are the same in that wavelength range (see equations 23 and 24) and the inferred RFED scales only with the luminosity of the central source at the different wavelengths. For $\lambda > 1 \mu\text{m}$, the chosen wavelength steps are smaller between 1 and $2 \mu\text{m}$. Since $T_{\text{source}} = 2500 \text{ K}$, the emission from the central source peaks in that wavelength region while the dust opacity is still relatively high. As a consequence, a consistent fraction of source luminosity is absorbed or scattered within the system at those wavelengths. Therefore, a good sampling in that wavelength region is desirable to obtain a more accurate

solution for the dust temperature. At longer wavelengths, a finer sampling is not as important since both the opacity and the radiation intensity from the central source decrease rapidly.

After the RT calculation has been performed at all the wavelengths specified above, we obtained a grid of RFED spectra at each cell position. Then, we calculated the energy density values in the entire wavelength range $0.01\text{--}1 \mu\text{m}$ by scaling the value inferred at $\lambda = 0.443 \mu\text{m}$ according to the central source luminosity at different wavelengths. This is possible because for $\lambda < 1 \mu\text{m}$ the dust opacity is assumed to be constant. In the wavelength range $1\text{--}100 \mu\text{m}$ we simply interpolated the inferred values within that range. Then, in a way consistent with the DUSTY code calculation, we derived the equilibrium dust temperature T_d at each position such that

$$\int q_{\lambda,\text{abs}} B_{\lambda}(T_d) d\lambda = \frac{c}{4\pi} \int q_{\lambda,\text{abs}} U_{\lambda} d\lambda. \quad (28)$$

We also calculated the spectra of the outgoing radiation flux at the outer radius of the shell, a quantity given in the output of the DUSTY code, as follows. First, we derived the total escaping luminosity $L_{\lambda,\text{esc}}$ by taking advantage of the cell average escaping brightness $\langle I_{\lambda,\text{esc}} \rangle$ within each HEALPix main direction, as provided by our code (see Section 3.4). In fact, $L_{\lambda,\text{esc}}$ can be expressed as

$$L_{\lambda,\text{esc}} = \sum_i \langle I_{\lambda,\text{esc}} \rangle_i \Omega_{\text{HP,MS}}^i A_{\text{EM}}^i, \quad (29)$$

where the sum is performed for all the leaf cells and all the HEALPix main sectors. The outgoing flux can then be derived by simply dividing $L_{\lambda,\text{esc}}$ by $4\pi R_2^2$. In order to obtain the values of $L_{\lambda,\text{esc}}$ for a larger set of wavelengths, we used the same procedure already applied for the scaling and interpolation of the inferred RFED (see above). We also calculated the contribution to the outgoing flux due to dust emission, which we derived assuming that the dust in each layer of the shell emits accordingly to the dust temperature radial profile we derived. Finally, we summed up both the central source and dust emission contributions to obtain the total outgoing radiation spectra.

In Figs 9–16 we show the comparison of the dust temperature radial profiles and outgoing radiation spectra we inferred with our code with those obtained by the DUSTY code. Figs 9 and 10 show the results for the constant density profile for the ‘dust temperature’ test. As shown in Table 4, the average difference between the DUSTY code dust temperature profile and the one generated by our code is about 1–2 per cent for all the values of T_1 . The average difference between the inferred outgoing spectra is about 2 to 3 per cent for the points actually calculated by our code (triangles in the figure, hereafter referred to as ‘calculated fluxes’). In this estimate of the discrepancy we did not consider the near-infrared points which are dominated by dust emission). The discrepancy increases to 5–7 per cent if one consider the entire UV-to-IR SED we derived as explained above. The highest discrepancies are observed in the MIR region. An excess of flux in the MIR range is expected since we did not take into account dust self-attenuation in our code and dust opacity is still relatively high at MIR wavelengths. For the power-law density profile, the discrepancy between the inferred temperature profiles/SEDs increases while going to higher values of T_1 , as shown in Figs 11 and 12. Specifically, the average difference between the inferred dust temperature profiles is equal to 1.6, 2.3 and 3.4 per cent for T_1 equal to 200, 400 and 800 K, respectively. We note that the discrepancy is due to a systematic underestimation of the dust temperature by the 3D code, which is also expected because we did not include the extraheating due to self-absorption.

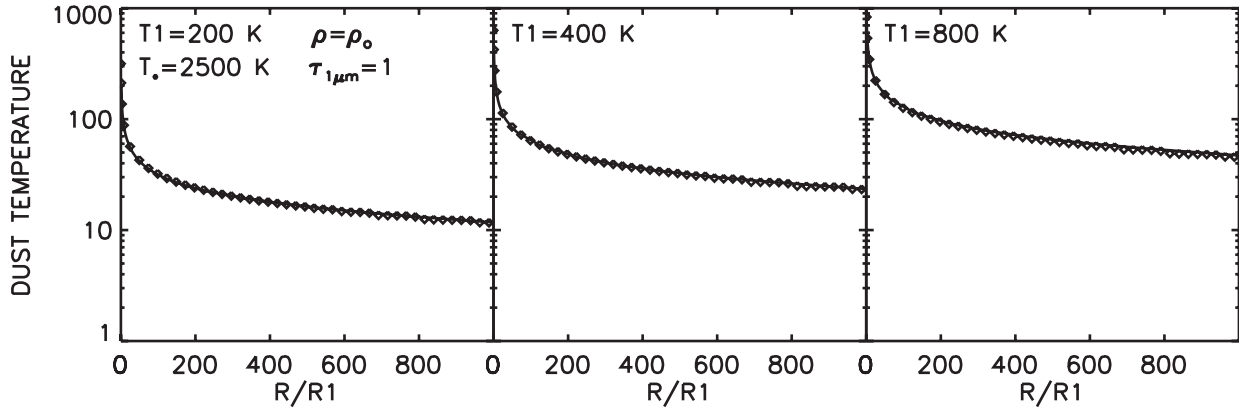


Figure 9. Dust temperature radial profile in the constant dust density case and for the ‘dust temperature’ tests. The plotted diamond symbols represent the temperature values inferred by our code. The continuous line is the DUSTY code solution.

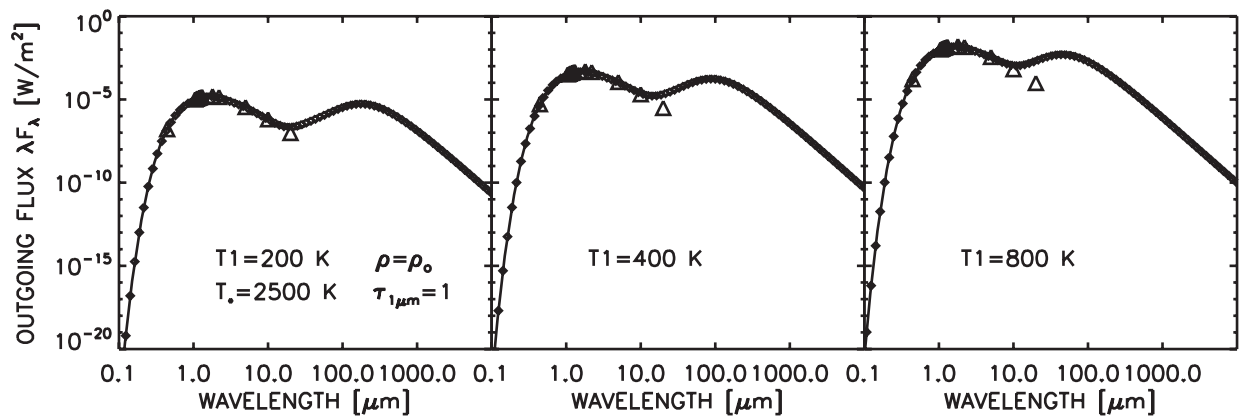


Figure 10. Outgoing radiation flux in the constant dust density case and for the ‘dust temperature’ tests. The plotted triangles represent the outgoing fluxes, for the radiation originating from the central source, inferred by our 3D RT calculations (note that the plotted values do not include the dust emission). The diamonds represent the sum of the interpolation of the fluxes calculated by our code at different wavelengths (see the text for details) plus the dust emission outgoing flux derived from the inferred dust temperature radial profile. The continuous line is the DUSTY code solution.

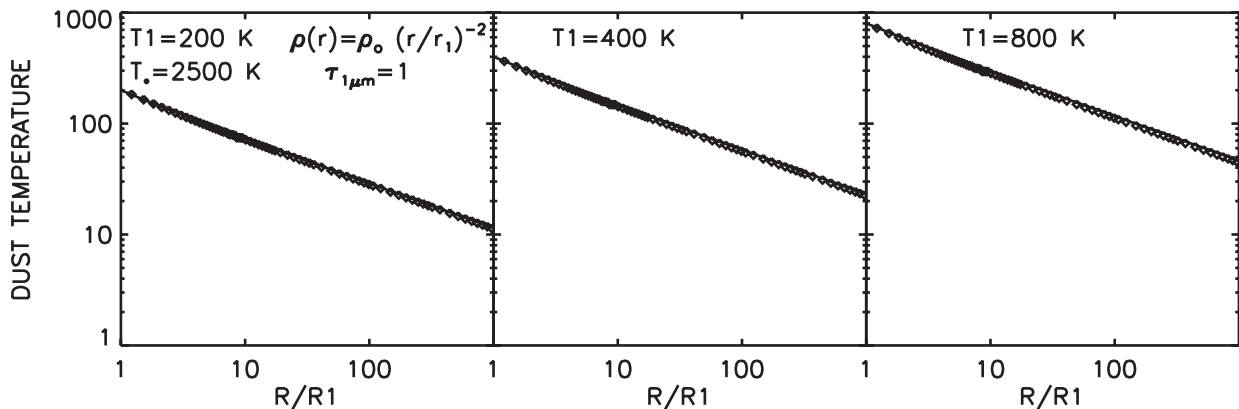


Figure 11. Dust temperature radial profile in the case of the power-law dust density profile and for the ‘dust temperature’ tests. Same symbols as in Fig. 9.

For the outgoing radiation spectra the average difference is in the range 2–4 per cent for the calculated fluxes and about 5–13 per cent for the global SEDs, with the highest discrepancies again in the MIR range.

The results of these tests show that there is only a rather small difference for the dust temperature radial profile inferred by the two codes for models at fixed optical depth $\tau_1 = 1$ and with dust temperature T_1 varying between 200 and 800 K. However, the discrepancy is higher for the outgoing spectra.

Figs 13–16 show the results for the ‘optical depth’ tests for the constant and power-law dust density profiles. Average discrepancies are tabulated in Table 5. In the case of the constant density profile (see Figs 13–14), all the three models ($T_1 = 200$ and $\tau_1 = 2, 5$ and 10) present an average difference for the dust temperature profiles of the order of 2 per cent. The outgoing radiation spectra differ on average by 5–17 per cent for the calculated fluxes and 9–29 per cent for the total SEDs. For the power-law profile, the average differences in the temperature profiles are 3.2, 6.5 and 15 per cent going from

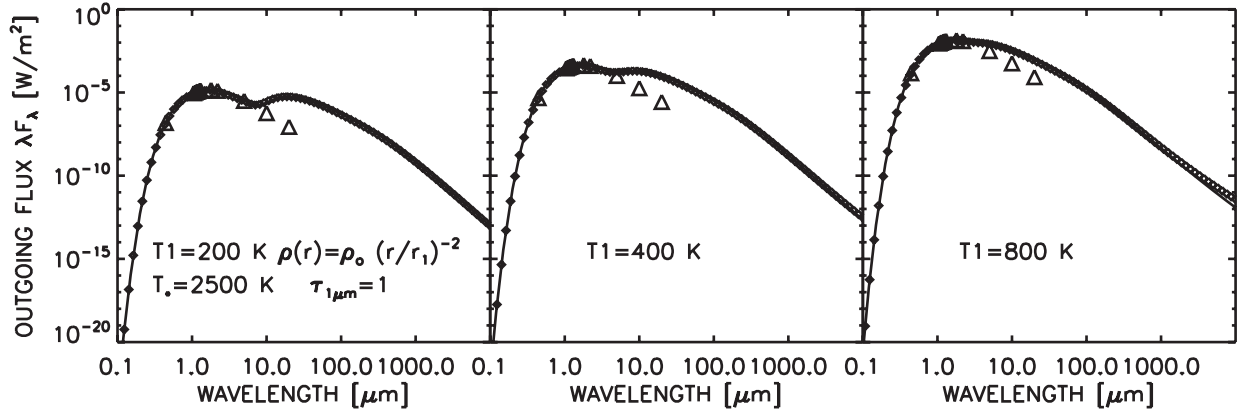


Figure 12. Outgoing radiation spectra in the case of the power-law dust density profile and for the ‘dust temperature’ tests. Same symbols as in Fig. 10.

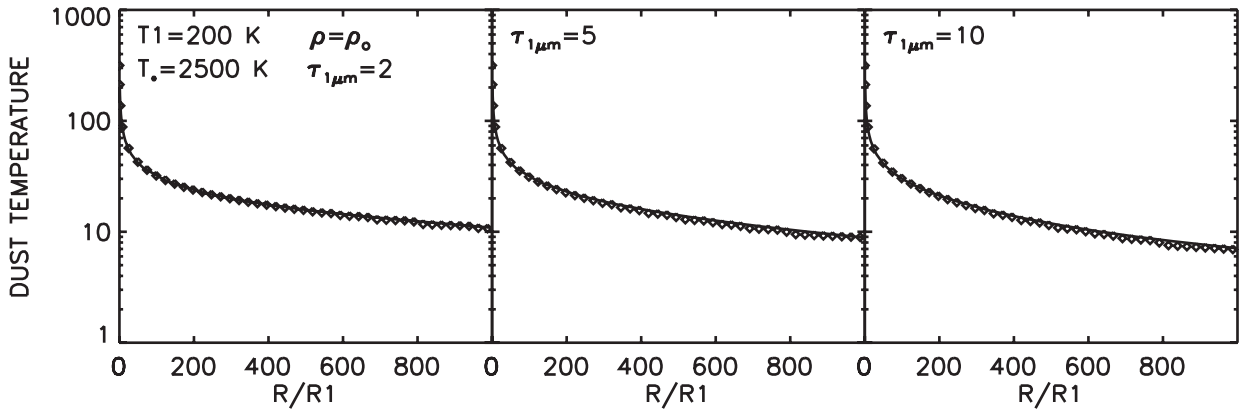


Figure 13. Dust temperature radial profile in the constant dust density case and for the ‘optical depth’ tests. Same symbols as in Fig. 9.

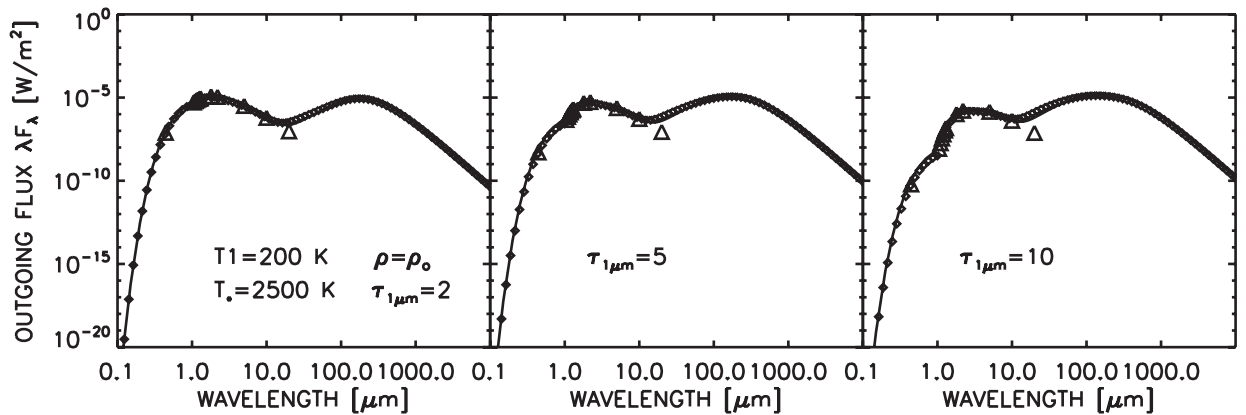


Figure 14. Outgoing radiation spectra in the constant dust density case and for the ‘optical depth’ tests. Same symbols as in Fig. 10.

$\tau_1 = 2$ to 10. Instead the differences for the outgoing radiation spectra are within 6–16 per cent for the calculated fluxes and 8–30 per cent for the total inferred SEDs. The discrepancy increases systematically with the optical depth of the model considered.

To summarize, from the comparison with the *DUSTY* code we obtained the following results. For the dust temperature test, we found that:

(i) – the dust temperature radial profile and the calculated fluxes agree within few per cent for both the constant and power-law dust density profile and

(ii) – the average discrepancy for the total SEDs is of the order of 5–10 per cent, with the highest discrepancies in the MIR region.

For the optical depth test, we found that:

(i) – the dust temperature radial profiles agree within few per cent for the constant dust density case, while for the power-law case the discrepancy increases with the optical depth of the model (up to 15 per cent for $\tau_1 = 10$) and

(ii) – the discrepancy for both the calculated fluxes and the total SEDs increases with the model optical depth in a similar way for both the dust density profiles. For the highest optical depth

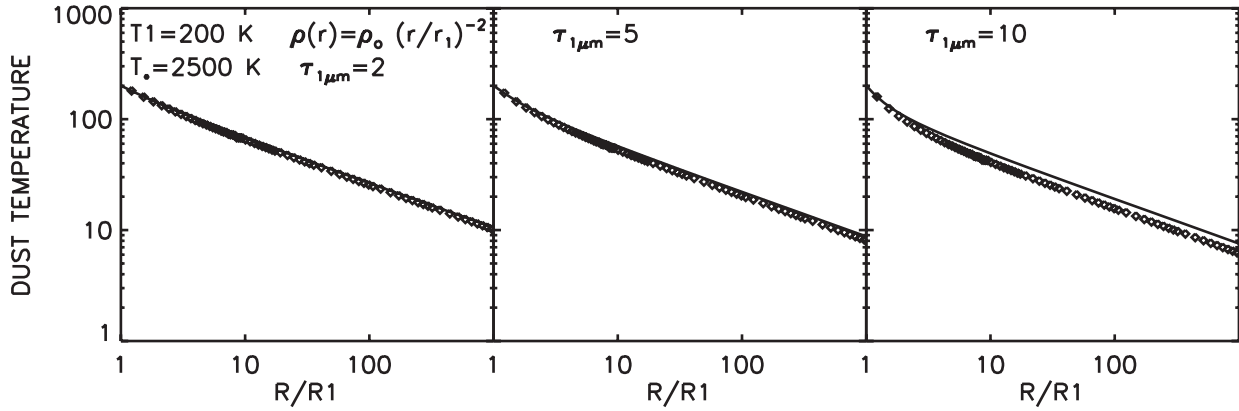


Figure 15. Dust temperature radial profile in the case of the power-law dust density profile and for the ‘optical depth’ tests. Same symbols as in Fig. 9.

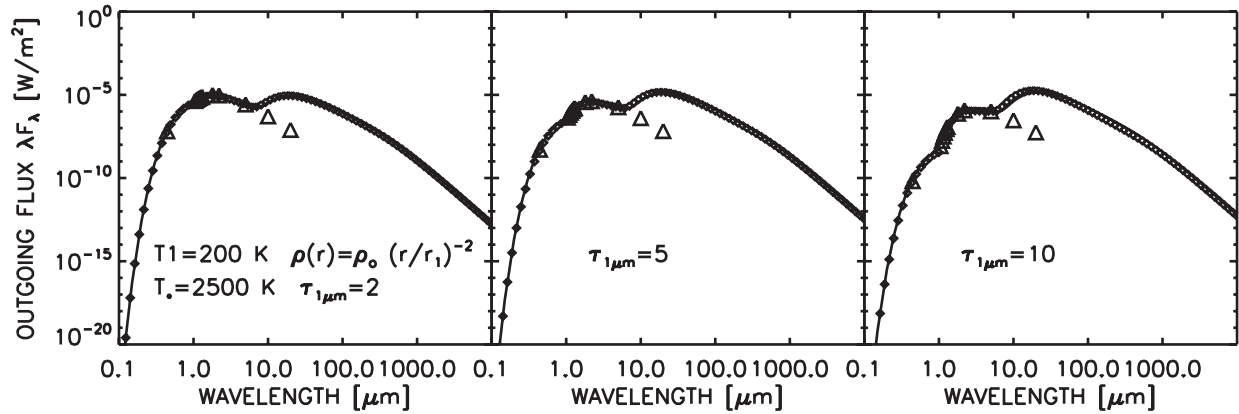


Figure 16. Outgoing radiation spectra in the case of the power-law dust density profile and for the ‘optical depth’ tests. Same symbols as in Fig. 10.

Table 4. Average relative discrepancies for the models of the ‘dust temperature test’: Column (1) $p = 0$ for the constant density model and $p = 2$ for the power-law model. Column (2) inner shell dust temperature. Columns (3)–(5) average relative discrepancy for the dust temperature radial profile, the calculated fluxes and the global SEDs (see the text).

| p | T_1 | $\langle \frac{\Delta T}{T} \rangle$ | $\langle \frac{\Delta \lambda F_\lambda}{\lambda F_\lambda} \rangle_{\text{CALC}}$ | $\langle \frac{\Delta \lambda F_\lambda}{\lambda F_\lambda} \rangle_{\text{SED}}$ |
|-----|-------|--------------------------------------|------------------------------------------------------------------------------------|-----------------------------------------------------------------------------------|
| 0 | 200 K | 0.018 | 0.025 | 0.07 |
| 0 | 400 K | 0.017 | 0.035 | 0.05 |
| 0 | 800 K | 0.01 | 0.03 | 0.068 |
| 2 | 200 K | 0.016 | 0.024 | 0.052 |
| 2 | 400 K | 0.023 | 0.03 | 0.063 |
| 2 | 800 K | 0.034 | 0.043 | 0.13 |

$\tau_1 = 10$, it is of the order of 15 per cent for the calculated fluxes and 30 per cent for the total SEDs. As before, the highest discrepancies when comparing the total SEDs are found in the MIR region.

Although the results provided by the two codes seem to be quite consistent for models with optical depths $\tau_1 = 1$ and 2, there is still some residual discrepancy for more optically thick models. A certainly important cause of the observed discrepancy is that, as already pointed out before, dust self-heating needs to be included in the code in order to predict accurate dust temperature profiles and output spectra, especially in the MIR region. However, another source of error is also the relatively low resolution of the 3D calculation compared to the 1D one. As explained before, the 3D grid

Table 5. Average relative discrepancies for the ‘optical depth test’: Column (1) $p = 0$ for the constant density model and $p = 2$ for the power-law dust density model. Column (2) radial optical depth at $1 \mu\text{m}$. Columns (3)–(5) average relative discrepancy for the dust temperature radial profile, the calculated fluxes and the global SEDs (see the text).

| p | τ_1 | $\langle \frac{\Delta T}{T} \rangle$ | $\langle \frac{\Delta \lambda F_\lambda}{\lambda F_\lambda} \rangle_{\text{CALC}}$ | $\langle \frac{\Delta \lambda F_\lambda}{\lambda F_\lambda} \rangle_{\text{SED}}$ |
|-----|----------|--------------------------------------|------------------------------------------------------------------------------------|-----------------------------------------------------------------------------------|
| 0 | 2 | 0.019 | 0.052 | 0.087 |
| 0 | 5 | 0.022 | 0.14 | 0.2 |
| 0 | 10 | 0.021 | 0.17 | 0.29 |
| 2 | 2 | 0.032 | 0.064 | 0.08 |
| 2 | 5 | 0.065 | 0.14 | 0.15 |
| 2 | 10 | 0.15 | 0.16 | 0.3 |

spatial resolution is higher in regions with higher dust density but it has been limited to keep the total number of cells in the range 10^5 – 10^6 . Thus, in the grids used in the calculations some regions have relatively high optical depths (see maximum cell optical depths in Table 3). An increased spatial resolution would have been beneficial to improve the accuracy of the solution but at the expense of a much longer computational time. This problem is more important for models with higher optical depths and might explain the residual discrepancy for the calculated fluxes in the UV–optical regime.

Because of the lack of dust self-heating in our code and the RT geometry assumed in this test, the solutions provided by the DUSTY

code do not provide ideal benchmarks to test our code. In particular, the geometry of the emission source/opacity of a star/dust shell does not resemble that of a galaxy, which is the class of object for which we developed our algorithm. For these reasons, we decided to compare solutions for a galaxy type geometry of stars and dust, using the 2D calculations of Popescu et al. (2011). The results of this comparison are shown in the next subsection.

5.2 Comparison with 2D calculations of Popescu et al. (2011)

Most of the dust RT solutions considered as benchmarks in the literature (e.g. Ivezić et al. 1997; Pascucci et al. 2004) are designed to test RT codes in cases resembling star-forming clouds or protoplanetary discs. Those systems can be well approximated by a central luminous source illuminating a spherical dust distribution or a dusty disc. Although able to handle completely arbitrary geometries, our code has been designed for the purpose of solving the RT problem in a galaxy-type geometry, which consists of an extended distribution of sources illuminating a dust distribution. For this reason, we decided to perform a comparison with the 2D RT calculations presented by Popescu et al. (2011, P11), which assume a disc galaxy geometry. The accuracy of the solutions for the radiation fields from P11 have been tested in Popescu & Tuffs (2013) against analytic solutions. For the cases where the analytic solution is an exact solution, the accuracy of the 2D code has been proven to be better than 1 per cent.

P11 used a modified version of the Kylafis & Bahcall (1987) 2D ray-tracing code to calculate radiation fields within a galaxy model comprising of three stellar components (a bulge, a disc and a thin disc) and two dust discs (called ‘thick dust disc’ and ‘thin dust disc’). Both the stellar volume emissivity and dust density for the disc-type components are described by a double exponential distribution:

$$f(R, z) = f(0, 0) \exp\left[-\frac{R}{h_{d,s}} - \frac{|z|}{z_{d,s}}\right], \tag{30}$$

where $h_{d,s}$ and $z_{d,s}$ are the scalelength and scaleheight of the disc components. As described in P11, the stellar discs (referred to as ‘disc’ for the old stellar component and ‘thin disc’ for the young stellar component) are characterized by the geometrical parameters scalelength and scaleheight, as reported in table E1 of that paper. They are also described by two parameters *old* and *SFR*. The *SFR* is a parameter defining the luminosity of the young stellar population (the thin disc) and *old* is a parameter defining the luminosity of the old stellar population (the disc). The spectral luminosity densities corresponding to the unit values of these parameters, $SFR = 1 M_{\odot} \text{ yr}^{-1}$ and $old = 1$ are given in table E2 of P11.¹¹ The parameter values for the stellar discs in the *B* band and the dust discs are also shown in Table 6, since they are used in the RT calculations we present below. The scaling of the dust density double exponential distributions is determined by the face-on central optical depth in the *B* band τ_B^f . For the galaxy model of P11, a fixed ratio equal to 0.387 is assumed for the face-on central optical depths of the thick dust disc and thin dust disc (see equation 10 in P11). The assumed opacity and scattering coefficients are those for $R_V = 3.1$ from Weingartner & Draine (2001), revised by Draine & Li (2007). Note that, unlike the comparison with the *DUSTY* code, the scattering is considered anisotropic in this case.

¹¹ We note that the models are truncated at the radius $R = 24$ kpc. The unit luminosities in table E2 of P11 refer to the luminosities within the truncation radius.

Table 6. Geometrical parameters of the disc and thin disc, together with the corresponding luminosity parameters for $old = 1$ and $SFR = 1 M_{\odot} \text{ yr}^{-1}$. All the values for the stellar discs are those for the *B* band. h_s^{disc} and z_s^{disc} : scale height/length for the old stellar disc; h_s^{tdisc} and z_s^{tdisc} : scale height/length for the young stellar disc; h_d^{disc} and z_d^{disc} : scale height/length for the thick dust disc; h_d^{tdisc} and z_d^{tdisc} : scale height/length for the thin dust disc; L_v^{disc} and L_v^{tdisc} : luminosity density for the old and young stellar disc, respectively.

| | |
|----------------------|------------------------------------------|
| h_s^{disc} | 5670 pc |
| z_s^{disc} | 419.58 pc |
| h_s^{tdisc} | 5670 pc |
| z_s^{tdisc} | 90.72 pc |
| h_d^{disc} | 7972.02 pc |
| z_d^{disc} | 272.16 pc |
| h_d^{tdisc} | 5670 pc |
| z_d^{tdisc} | 90.72 pc |
| L_v^{disc} | $4.771 \times 10^{21} \text{ W Hz}^{-1}$ |
| L_v^{tdisc} | $2.271 \times 10^{21} \text{ W Hz}^{-1}$ |

For the comparison between the solutions provided by the two codes, we used the library of radiation fields presented in Popescu & Tuffs (2013, PT13). From the library we obtained the contribution of the old stellar disc and young stellar disc to the RFED distribution separately, thus allowing a more careful check on the accuracy of the 3D calculation.

As for the comparison with the *DUSTY* code, the first step is to create the grids used in the calculations. We input in the grid creation algorithm (see Section 3.1) the functional shapes for the stellar and dust discs and impose the following criteria for the cell subdivision: (1) a maximum value for cell optical depth; (2) a maximum value for the cell luminosity; (3) a maximum cell subdivision level (typically about 6–7); (4) a subdivision level equal to the maximum subdivision level for the cells in the region close to the galaxy centre ($|z| < 1000$ and $R < 500$). By using condition (4), we required a higher spatial resolution in the galaxy central regions. Those regions are the ones where we expect the radiation field to vary more rapidly. An alternative way to obtain an increase of the spatial resolution in those regions would be by lowering further the threshold values for e.g. the cell optical depth required for the cell subdivision. However, this usually results in a substantial increase of the total number of cells even for relatively small changes for the required thresholds. For simplicity we decided to impose a condition simply based on the distance from the axis origin.

For each leaf cell we assigned for both the dust density and stellar volume emissivity the values averaged over the cell volume. That is, we numerically integrated the double exponential functions $f(R, z)$ describing the stellar and dust distribution within the cell volume V_c and then divided by V_c . That is

$$\langle f_c \rangle = \frac{\int_{V_c} f(R, z) \text{ dx dy dz}}{V_c}. \tag{31}$$

As mentioned above, we performed 3D calculations for the models including either the old stellar disc or the young stellar disc. The details and results of these tests are described in the following two subsections.

Table 7. 3D grid parameters for the comparison with the 2D calculations of P11. Column (1) stellar population considered in the calculation, OLD refers to the old stellar disc and YOUNG to the young stellar disc. Columns (2) and (3) maximum and average cell optical depth. Columns (4) and (5) maximum and average cell luminosity. Column (6) total number of cells.

| Model | $\Delta\tau_{B,\max}$ | $\langle\Delta\tau_B\rangle$ | $\frac{\Delta L_{B,\max}}{10^{17} \text{ W Hz}^{-1}}$ | $\langle\Delta L_B\rangle$ $10^{17} \text{ W Hz}^{-1}$ | N_{cells} |
|--------------|-----------------------|------------------------------|-------------------------------------------------------|-----------------------------------------------------------|--------------------|
| OLD (1, 3) | 0.4 | 0.047 | 4.76 | 0.46 | 109 620 |
| OLD (2) | 0.28 | 0.048 | 4.76 | 0.50 | 97 200 |
| YOUNG (1, 2) | 0.4 | 0.059 | 2.27 | 0.25 | 95 040 |

5.2.1 Calculations for the old stellar disc

We considered the old stellar disc of the P11 galaxy model for $old = 1$ and we calculated the RFED distribution in the B band for the following models (maximum and average cell optical depth and luminosity in Table 7. For all the models we used $f_U = 10^{-7}$, $N_{\text{rays}} = 2$ and $f_L = 10^{-3}$):¹²

- (1) $\tau_B^f = 0$ (optically thin model);
- (2) $\tau_B^f = 1$, only the thick dust disc;
- (3) $\tau_B^f = 1$, both the thick and thin dust discs.

Model (1) has been calculated to check the accuracy of the 3D code when dust is not included. Fig. 17 shows a comparison of the RFED radial and vertical profiles obtained by this calculation (diamonds symbols) and by the 2D code used by P11 (continuous line, same convention hereafter). For the comparison we selected the vertical profiles at $R = 0, 5, 10, 18$ kpc and radial profiles at $z = 0, 400, 1000, 2000$ pc (note that while the plots for $R = 0$ and $z = 0$ pc show the exact values obtained from the 3D calculation, the other plots show values obtained through interpolation within the 3D grid). As shown in Table 8, the average discrepancy for the vertical profiles is of the order of 1–2 per cent for $R = 0, 5, 10$ kpc and about 5 per cent for $R = 18$ kpc. For the radial profiles the discrepancies are between 2 and 5 per cent, although most of the disagreement is found at large radial distances.

Model (2) includes only the thick dust disc but not the thin dust disc. We calculated this model because both the old stellar disc and the thick dust disc can be well resolved by an adaptive grid containing of the order of 10^5 cells. Resolving the thin dust disc properly requires an order of magnitude more cells and this is avoided in this calculation to reduce the calculation time (but see model 3 below). Because the thin dust disc is not present, all the opacity is assigned to the thick dust disc (at variance with the original P11 galaxy model). For this test we show three sets of results. Fig. 18 shows the profile of the radiation field including only the direct light from the stellar distribution. Fig. 19 includes the direct light and the first order scattered light. This calculation has been performed since the 2D code of P11 is based on an algorithm which explicitly calculates only the first order scattered light, assuming that the ratio between the specific intensity of successive scattering orders is constant (see Kylafis & Bahcall 1987 for more details). Thus, it is important to verify the agreement at this stage before comparing the final solution including all order scattering, shown in Fig. 20. The calculations including only direct light agree within 1–4 per cent for both vertical and radial profiles. The agreement for the solution including also the first order scattered light is within about 0.5–

2 per cent for the vertical profiles and within 1–3 per cent for the radial profiles. Finally, the comparison for the solution including all order scattered light shows an agreement within 1–2 per cent for the vertical profiles and 2–3 per cent for the radial profiles.

For model (3) the calculations include both dust discs, although the thin dust disc is not well resolved especially at large radii (cell sizes on the galaxy plane varying between 65 and 592 pc, while the scaleheight of the thin dust disc is about 91 pc). Similarly as before, Figs 21–23 show the solutions for the RFED profiles including the direct light, the direct light plus the first order scattered light and the final values including all scattered light, respectively. The comparison for the direct light shows an agreement within about 2–6 per cent while the calculations including direct light and first order scattered light agree within 1–4 per cent. For the last calculation including all the stellar and scattered light contributions to the RFED, the average discrepancies are within 1–4 per cent for the vertical profiles, about 7 per cent for the radial profile at $z = 0$ pc and about 3–4 per cent for the radial profiles at $z = 400, 1000, 2000$ pc.

The 3D calculations performed for the old stellar disc show a good agreement with the 2D solutions, with the residual discrepancies being plausibly due to the resolution of the 3D grid which does not resolve properly the thin dust disc in the central regions and both the discs at large radii.

5.2.2 Calculations for the young stellar disc

3D calculations to obtain the RFED distribution due to the thin stellar disc are more challenging because, as previously stated, in order to properly resolve the young stellar and thin dust discs, one should in principle create a grid containing of the order of 10^6 cells. We preferred to use a grid of about 10^5 cells which underresolves the thin discs but it allows shorter computational times. The downside is that the 3D calculations will be less accurate numerically.

For this set of tests we considered a young stellar disc with $SFR = 1 M_{\odot} \text{ yr}^{-1}$ and we calculated the RFED in the B band for the following models (as before, we used $f_U = 10^{-7}$, $N_{\text{rays}} = 2$ and $f_L = 10^{-3}$):

- (1) $\tau_B = 0$ (optically thin case) and
- (2) $\tau_B = 1$, both dust discs.

Fig. 24 shows the results for model (1). The calculated vertical profiles from the 2D and 3D codes agree within 1–4 per cent for $R = 0, 5, 10$ kpc while the average discrepancy is about 10 per cent for $R = 18$ kpc (see Table 8). The discrepancies tend to be higher for the radial profiles, that is, about 5–10 per cent with most of the discrepancy found at large radii. However, in this case the discrepancy seems not to be due only to the coarse 3D grid resolution at large radii. In fact, the 2D calculation shows an artificial feature on the $R = 18$ kpc plot for low values of z . This feature is due to inaccuracies in the 2D calculation.

Fig. 25 shows the calculations for model (2). The average discrepancies are of the order of 3–6 per cent for the vertical profiles and about 5–7 per cent for the radial profiles. Note that the ‘steps’ appearing in the radial profile for $Z = 0$ are located at the position where the adaptive grid changes cell size. They appear also in the old stellar disc solutions but in a less evident way.

The 3D calculations for the young stellar disc provide solutions which still present a fairly good agreement, although there is a higher discrepancy compared to the old stellar disc calculations. As said before, this is most probably mainly due to the low resolution of the 3D grid, unable to properly resolve the stellar and dust components in this test.

¹² The choice of f_U and N_{rays} is such to guarantee global energy balance within a few per cent accuracy (see Section 4).

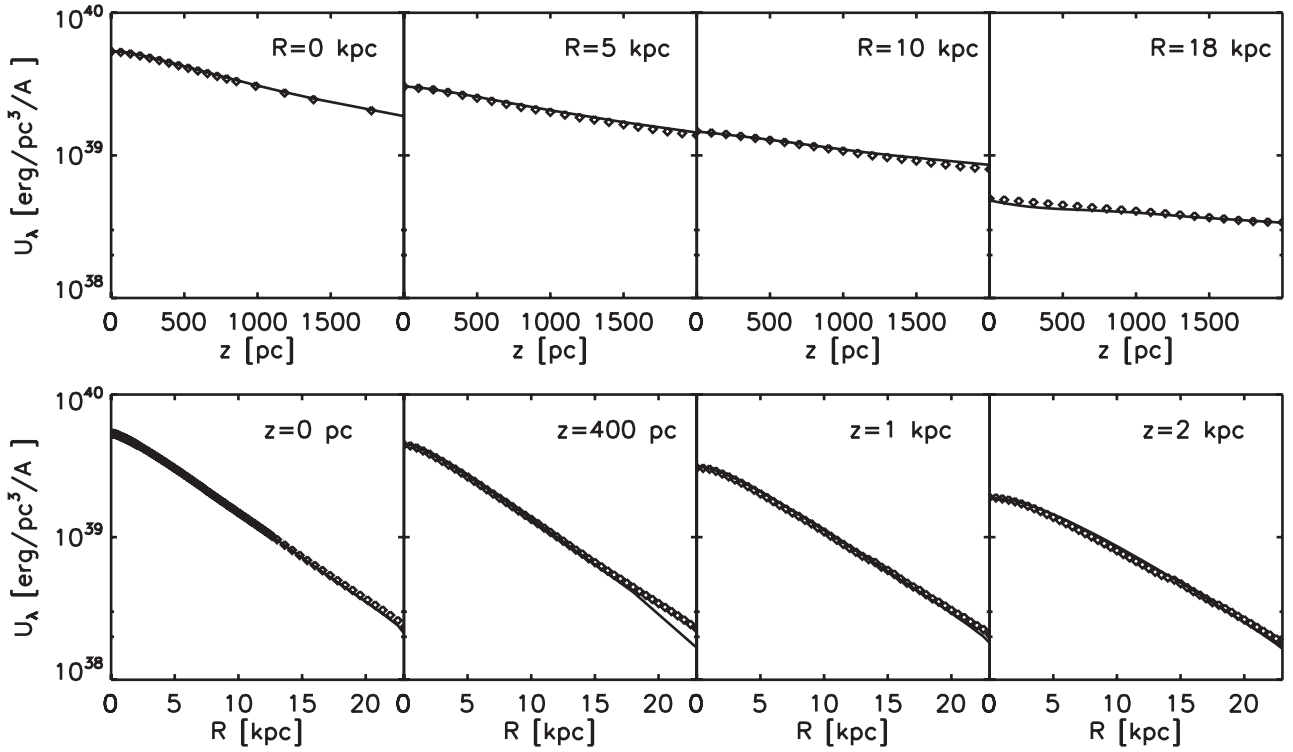


Figure 17. RFED radial and vertical profiles for the old stellar disc in the optically thin case, B band. Diamonds represent the RFED values calculated by our 3D code while the continuous line is the solution obtained by the 2D code of Popescu et al. (2011). The diamond symbols plotted in the $R = 0$ and $z = 0$ plots represent the exact values obtained by the 3D code. For all the other plots, the plotted values are obtained through interpolation within the 3D grid.

Table 8. Average relative discrepancies for the B -band RFED profiles calculated using our 3D code and those from the code of P11. Column (1) model calculated (see the text). Column (2) type of calculation: NODUST = optically thin case, DIR = only direct stellar light, DIR+SCA1 = only direct light and first order scattered light, ALL = direct and all order scattered light. Columns (3)–(6) average discrepancies for the RFED vertical profiles at $R_1 = 0$ kpc, $R_2 = 5$ kpc, $R_3 = 10$ kpc and $R_4 = 18$ kpc. Columns (7)–(10) average discrepancies for the RFED radial profiles at $z_1 = 0$ kpc, $z_2 = 400$ pc, $z_3 = 1$ kpc and $z_4 = 2$ kpc.

| Model | Type | $\langle \frac{\Delta U_\lambda}{U_\lambda} \rangle$ | | | | | | | |
|-----------|----------|------------------------------------------------------|-------|-------|-------|--------|-------|-------|-------|
| | | R_1 | R_2 | R_3 | R_4 | z_1 | z_2 | z_3 | z_4 |
| OLD (1) | NODUST | 0.009 | 0.02 | 0.02 | 0.048 | 0.017 | 0.046 | 0.036 | 0.036 |
| OLD (2) | DIR | 0.014 | 0.018 | 0.019 | 0.037 | 0.038 | 0.03 | 0.016 | 0.028 |
| OLD (2) | DIR+SCA1 | 0.019 | 0.008 | 0.006 | 0.022 | 0.014 | 0.029 | 0.017 | 0.024 |
| OLD (2) | ALL | 0.016 | 0.015 | 0.015 | 0.013 | 0.02 | 0.022 | 0.034 | 0.032 |
| OLD (3) | DIR | 0.03 | 0.04 | 0.054 | 0.068 | 0.0079 | 0.06 | 0.034 | 0.027 |
| OLD (3) | DIR+SCA1 | 0.014 | 0.01 | 0.02 | 0.034 | 0.027 | 0.036 | 0.021 | 0.023 |
| OLD (3) | ALL | 0.036 | 0.013 | 0.01 | 0.025 | 0.073 | 0.027 | 0.035 | 0.035 |
| YOUNG (1) | NODUST | 0.0078 | 0.02 | 0.043 | 0.095 | 0.055 | 0.097 | 0.066 | 0.027 |
| YOUNG (2) | ALL | 0.052 | 0.061 | 0.046 | 0.032 | 0.069 | 0.065 | 0.054 | 0.048 |

6 AN RT 3D APPLICATION: INCLUDING SPIRAL ARMS IN GALAXY MODELS

For most practical applications to large statistical samples of galaxies (e.g. Driver et al. 2007, 2008, 2012; Gunawardhana et al. 2011; Silva et al. 2011; Grootes et al. 2013), RT modelling of the observed spatially integrated direct and dust-reradiated starlight necessarily (in the absence of detailed images) adopts 2D axisymmetric approximation of the distribution of stars and dust. However, the distribution of light at UV and short optical wavelengths from young massive stars is well known in real galaxies to be biased towards

a spiral pattern of enhanced dust density, rather than the smooth exponential disc function typically assumed by these models. The question therefore arises whether this effect introduces any systematic bias into 2D model predictions of dust attenuation of integrated starlight and averaged RFED in spiral galaxies. To evaluate this bias, we have performed a RT calculation for a galaxy model including logarithmic spiral arms. We considered a typical model galaxy from P11, consisting of a disc with $old = 1$ and a thin stellar disc with $SFR = 1 M_\odot \text{ yr}^{-1}$, and two dust discs with $\tau_B^f = 1$ (see Section 5.2 for a description of the model parameters of P11). We modified this model using the same procedure as that adopted in P11 for

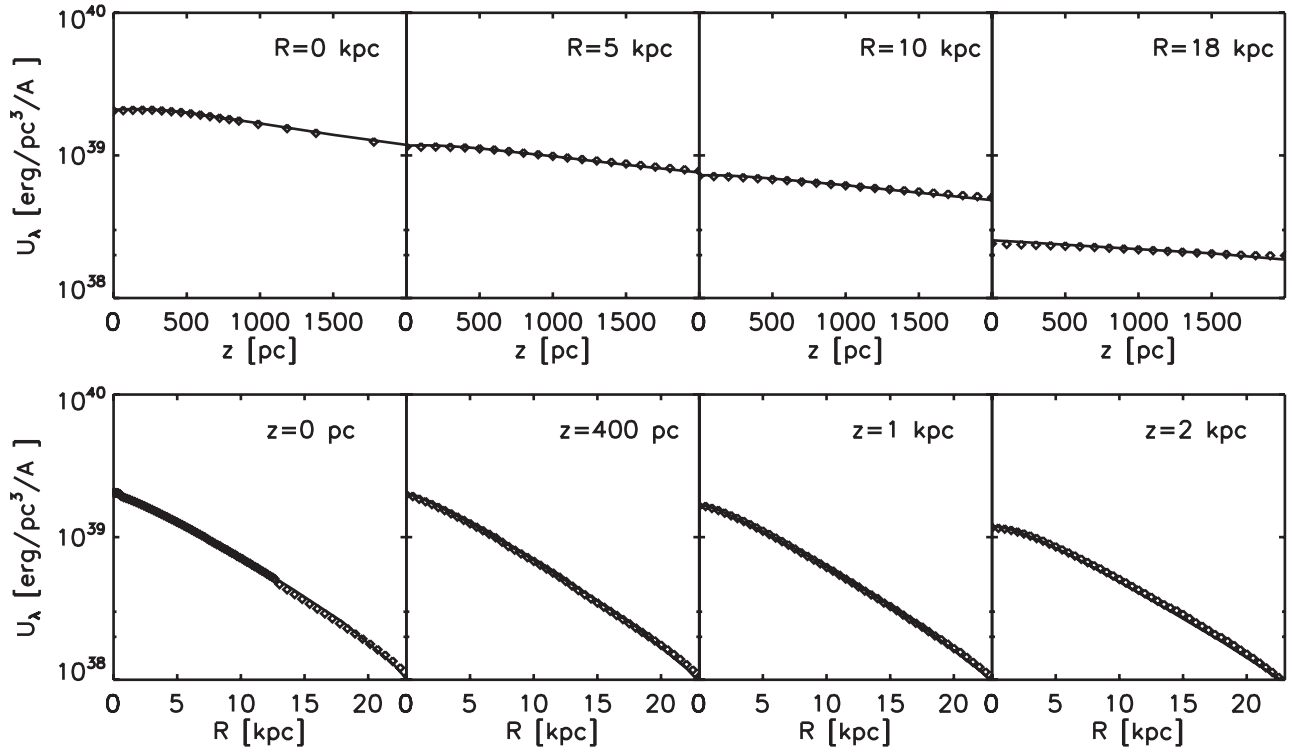


Figure 18. RFED radial and vertical profile for the old stellar disc for $\tau_B = 1$, B band. In this model, the thin dust disc is not included. Also, only the contribution from direct stellar light is considered. Same symbols as in Fig. 17.

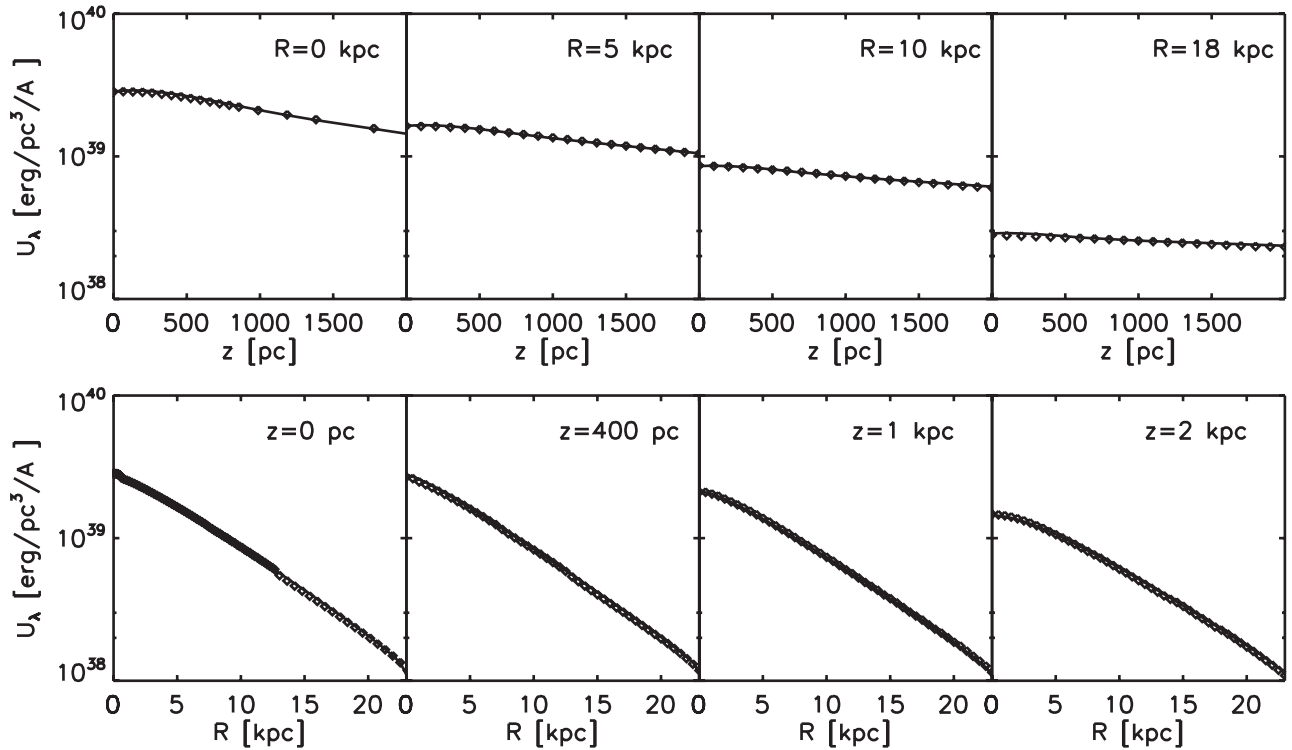


Figure 19. RFED radial and vertical profile for the old stellar disc for $\tau_B = 1$, B band. In this model, the thin dust disc is not included. Also, only the contributions from direct stellar light and the first order scattered light are included. Same symbols as in Fig. 17.

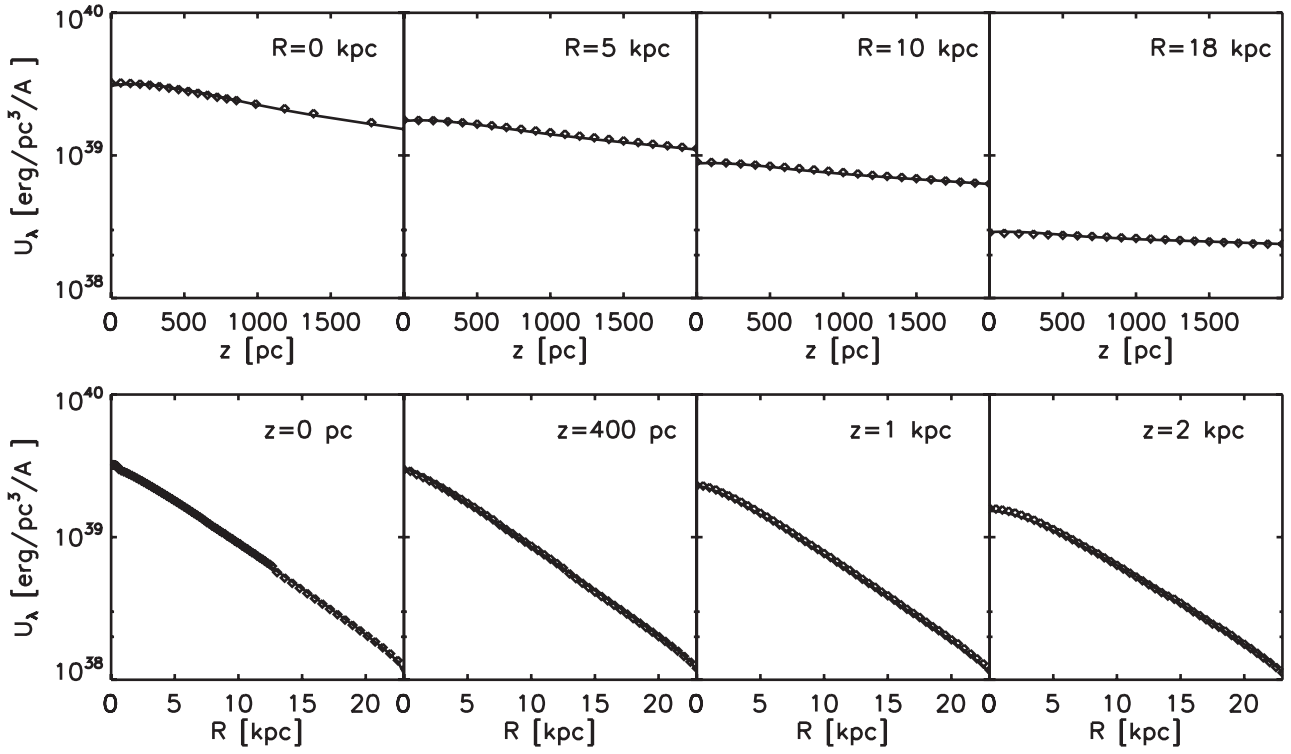


Figure 20. RFED radial and vertical profile for the old stellar disc for $\tau_B = 1$, B band. In this model, the thin dust disc is not included. Both direct stellar light and all order scattered light contributions are included. Same symbols as in Fig. 17.

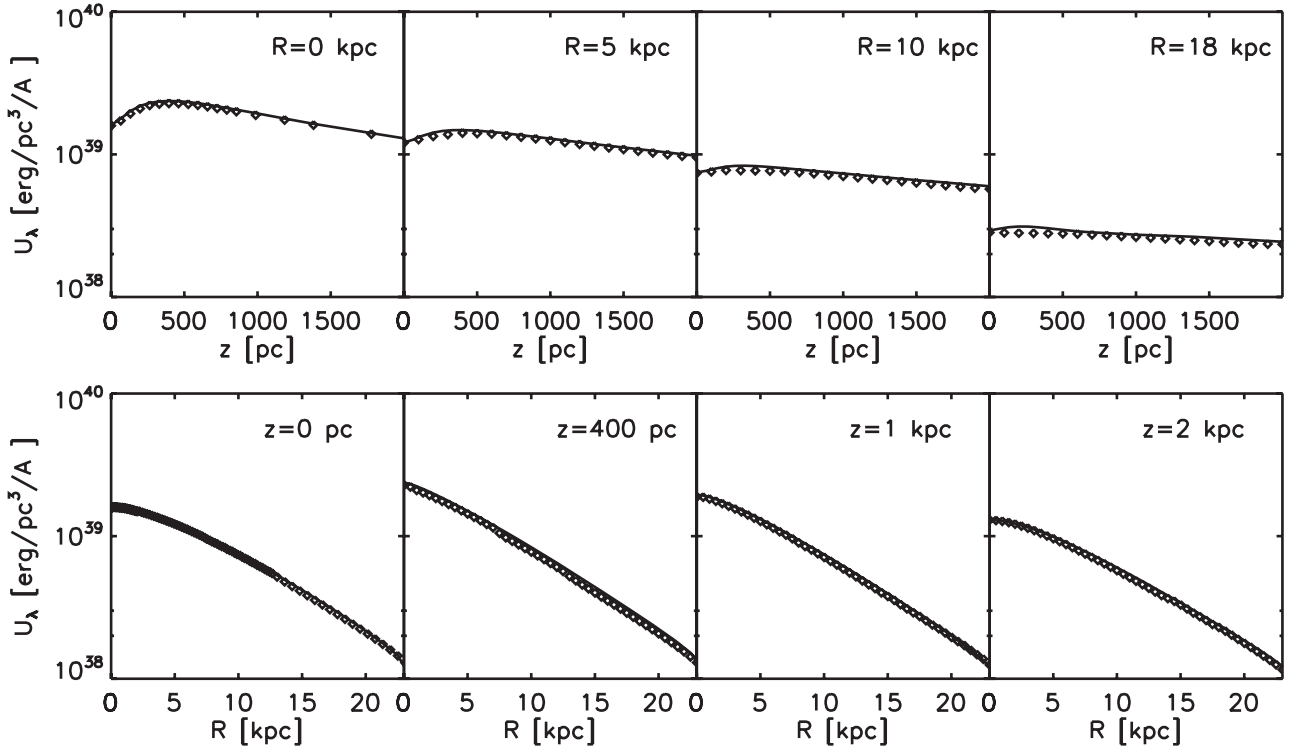


Figure 21. RFED radial and vertical profile for the old stellar disc for $\tau_B = 1$, B band with both the thick and thin disc included. Only direct stellar light is included. Same symbols as in Fig. 17.

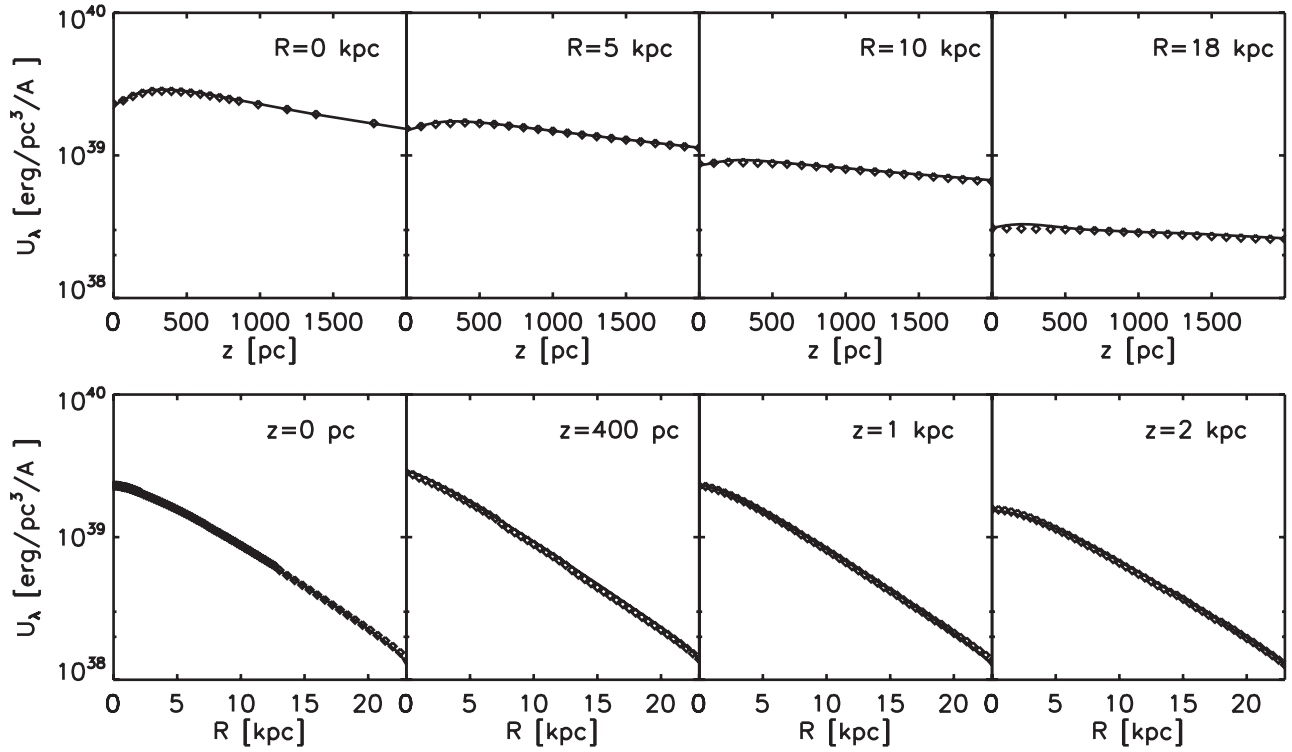


Figure 22. RFED radial and vertical profile for the old stellar disc for $\tau_B = 1$, B band with both the thick and thin disc included. Only direct stellar light and first order scattered light are included. Same symbols as in Fig. 17.

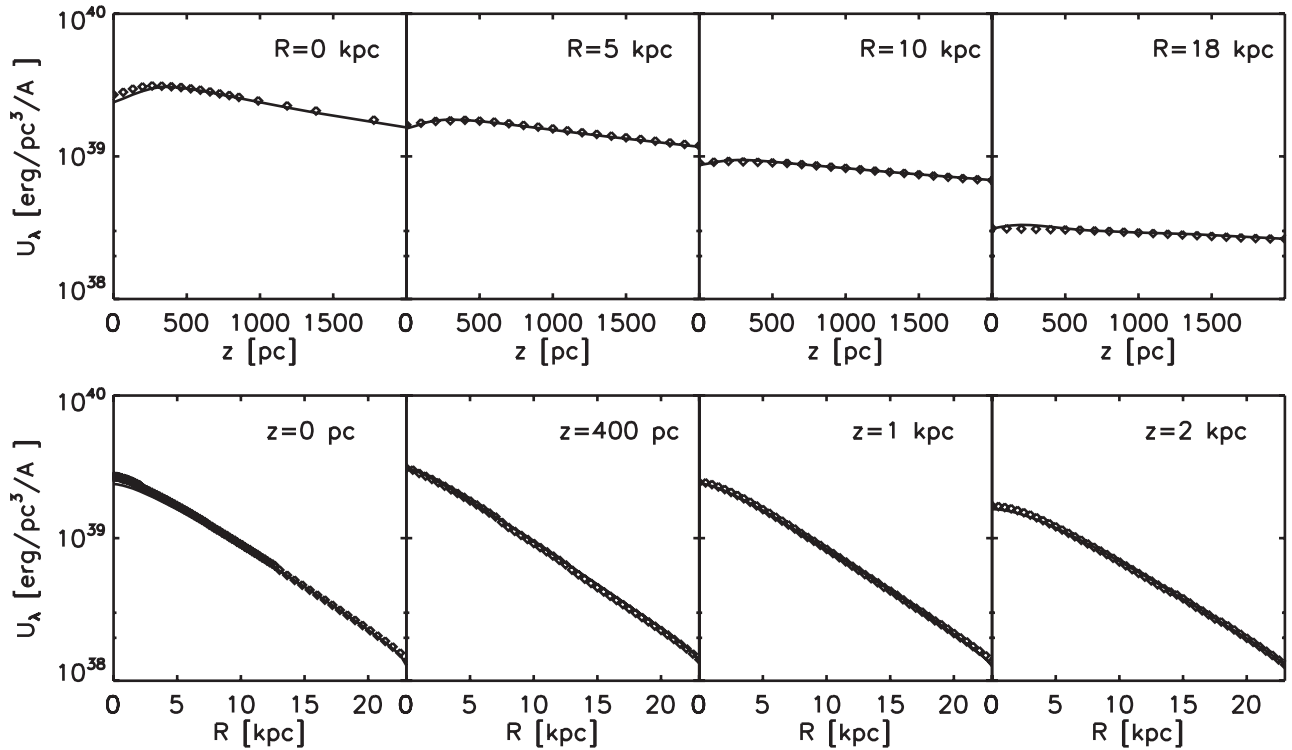


Figure 23. RFED radial and vertical profile for the old stellar disc for $\tau_B = 1$, B band with both the thick and thin disc included. Both direct stellar light and all order scattered light contributions are included. Same symbols as in Fig. 17.

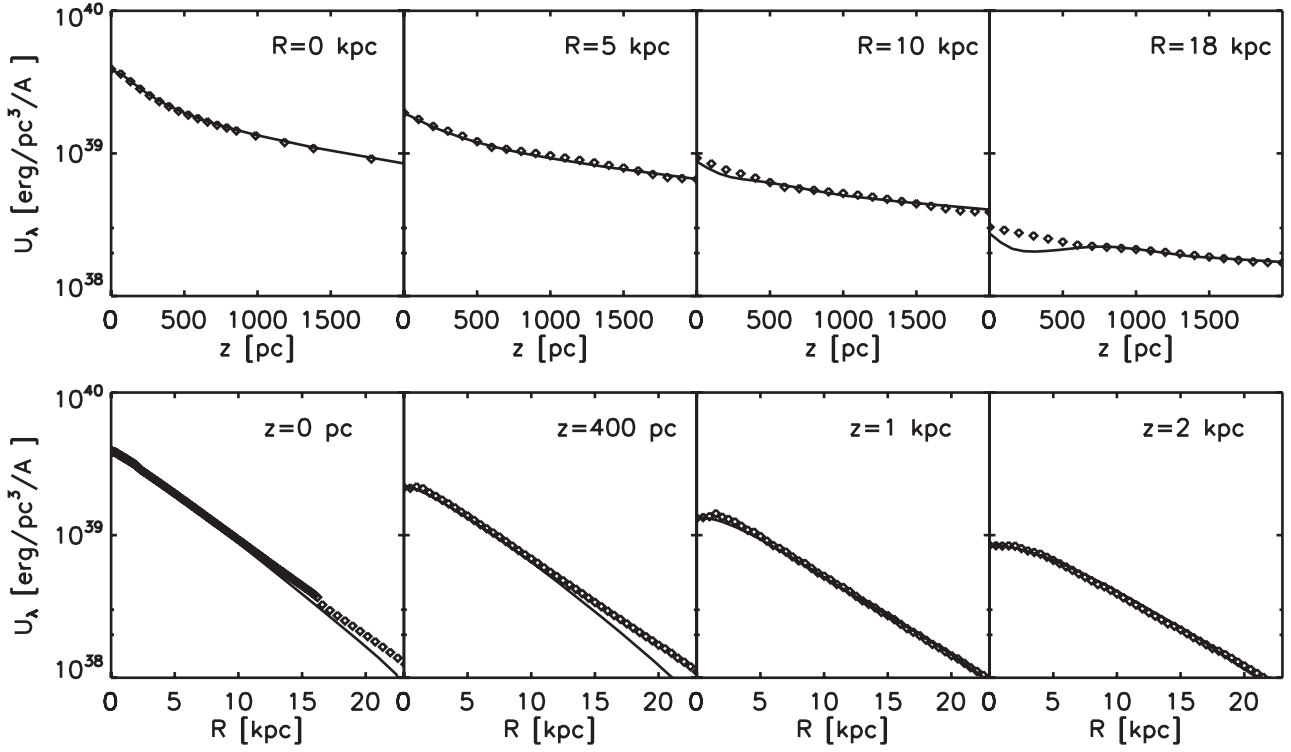


Figure 24. Radial and vertical profile for the young stellar disc in the optically thin case, B band. Same symbols as in Fig. 17.

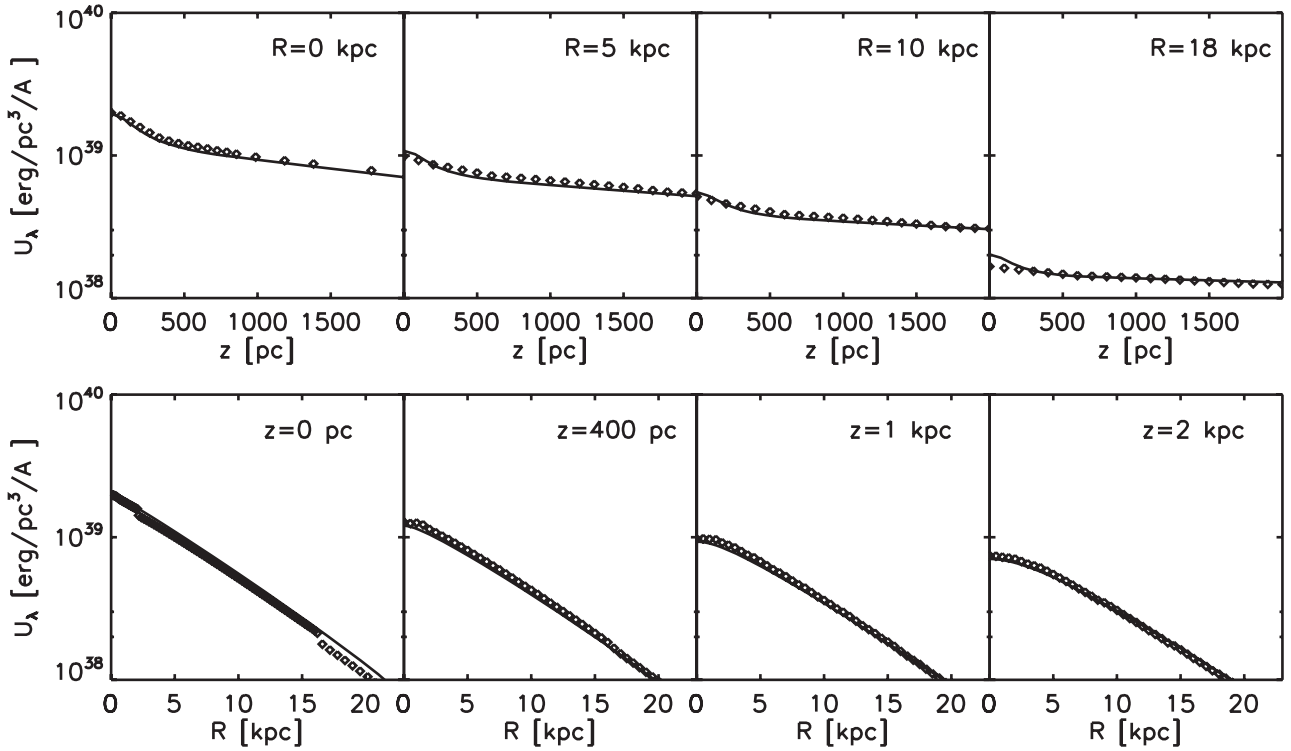


Figure 25. Radial and vertical profile for the young stellar disc for $\tau_B = 1$, B band. Same symbols as in Fig. 17.

the inclusion of circular spiral arms. Thus, we considered the same double exponential distribution for the thick stellar and dust disc but we redistributed the thin disc stellar luminosity and dust mass within spiral arms. As shown in Schechtman-Rook, Bershadsky &

Wood (2012), the implementation of logarithmic spiral arms can be done by multiplying a logarithmic spiral disc perturbation ξ to the double exponential formula describing the stellar volume emissivity and dust density (see equation 30). We adopted the expression for

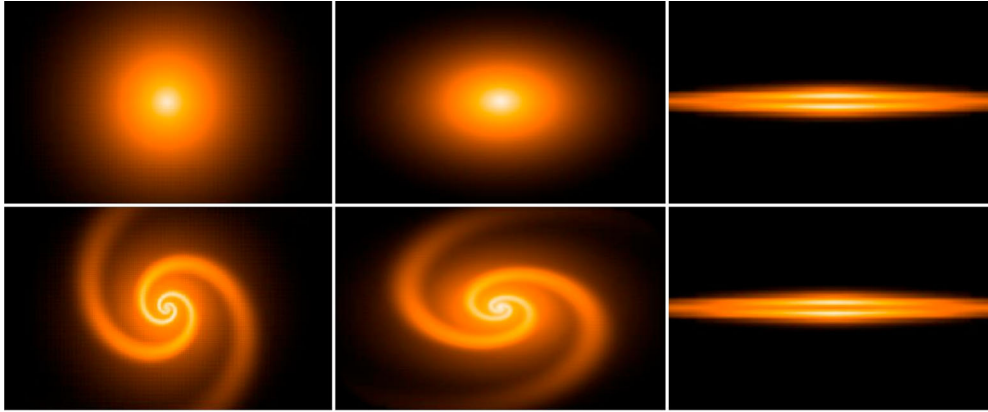


Figure 26. Comparison of the images of output surface brightness at different inclinations (0° , 51° and 90° from left to right) for a pure double exponential disc galaxy model (upper row) and a model including spiral arms (lower row). The models are for a central face-on optical depth $\tau_B^f = 1$. See the text for details.

ξ in their formula 10 (two spiral arms):

$$\xi = \left[1 - w + \prod_{n=2, n+2}^N \frac{n}{n-1} \sin^N \times \left(\frac{\ln(\sqrt{x^2 + y^2})}{\tan(p)} - \tan^{-1} \left(\frac{y}{x} \right) + \frac{\pi}{4} \right) \right], \quad (32)$$

with w the fraction of stellar light or dust within the spiral arms, p the pitch angle determining how tightly the spirals turn around each other and the exponent N which regulates the relative size of the arm and interarm regions. For these parameters, we adopted the values $w = 0.9$, $p = 10^\circ$ and $N = 10$. Then, we performed an RT calculation for a galaxy model (including both old and young stellar discs) in the B band with face-on central optical depth $\tau_B^f = 1$ and disc parameter values as in Table 6.

Fig. 26 shows the comparison for the output surface brightness images at different inclinations between a pure double exponential model (upper row) and for the model including spirals (lower row). The images show the different morphology of the stellar emission for the face-on and low-inclination images. However, the edge-on images are remarkably similar for the two models. We also made a comparison for the total attenuation as a function of galaxy inclination for the two models, which is shown in Fig. 27. The attenuation curves are quite close to each other, within 0.02 dex, showing that

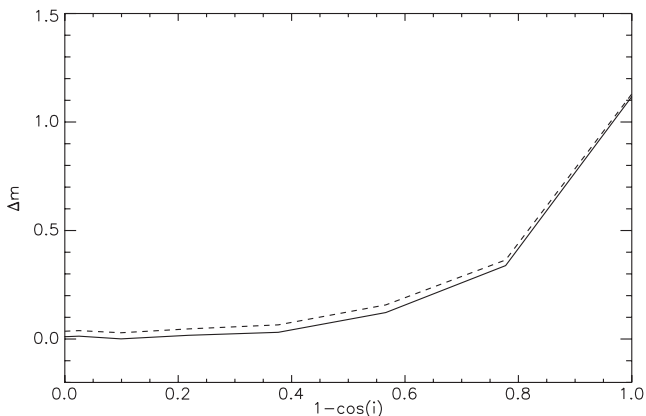


Figure 27. Comparison of the attenuation curves in the B band as a function of galaxy inclination for the pure double exponential model (continuous line) and for the model with spiral arms (dashed line).

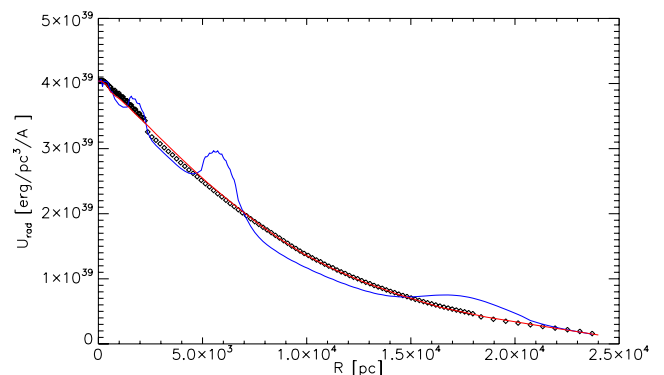


Figure 28. Comparison of the B -band RFED radial profile for the models with and without spiral arms. The squares represent the RFED values for the pure double exponential galaxy model. The blue line is the RFED profile along the x -axis of the spiral galaxy model, while the red line is the RFED profile azimuthally averaged for the same model.

the spiral pattern does not affect much the total attenuation of the galaxy for the adopted parameters.

Finally, we compared the RFED profiles in the galaxy plane. Fig. 28 shows the profiles for the pure double exponential model (squares), a cut along the x -axis of the model including spiral arms (blue line) and its azimuthally averaged RFED profile. Interestingly enough, although the RFED along the x -axis shows the variation due to the spiral arms, the azimuthally averaged profile is very close to the profile for the model without spiral arms.

Although P11 have already shown that the spatially integrated dust and PAH emission SED of a typical spiral galaxy does not depend on whether the young stellar population and associated dust is distributed in a circular spiral arm or in a disc, here we show for the first time that it is at the level of the radiation fields that heat the dust that the distributions in the spirals start to resemble the disc distributions on the average.

The results on the global attenuation, images and radiation fields, all suggest that double exponential models can be a quite good representation for spiral disc galaxies, and that the spatially integrated SEDs of spirals can be accounted by 2D models. Although this is in qualitative agreement with previous works (Misiriotis et al. 2000; Semionov et al. 2006; P11), a more extensive study is needed to see how the different parameters, e.g. the face-on optical depth, affect

the attenuation curve and the radiation fields in models with and without spiral arms.

7 SUMMARY AND OUTLOOK

In this paper we present a new ray-tracing dust radiation transfer algorithm which is able to handle arbitrary 3D geometries and it is specifically designed to calculate accurate RFED within galaxy models. The main optimization characteristics of this algorithm are the following:

- (1) an adaptive 3D grid (see Section 3.1);
- (2) a ray-tracing algorithm based on the pre-calculation of a lower limit for the RFED (see Sections 3.2 and 3.3);
- (3) an iterative procedure for the optimization of the angular density for the rays departing from each emitting cell (Section 3.3).

Furthermore, parallelized versions of the code have been written for its use on shared-memory machines and computer clusters.

In order to verify the code accuracy, we performed comparisons with the results provided by other codes. Specifically, we used our code to calculate solutions for a spherical dusty shell illuminated by a central point source and for an axis symmetric galaxy model. For the first configuration, we considered as benchmark a set of solutions calculated by using the *DUSTY* 1D code (Ivezic & Elitzur 1997). We showed that the equilibrium dust temperature radial profiles and the outgoing flux spectra derived by our 3D calculations agree within a few per cent with the benchmark solutions for models with low radial optical depths ($\tau_1 = 1, 2$) but present larger discrepancies for more optically thick models ($\tau_1 = 5, 10$). The residual discrepancies, especially for the models with higher optical depths, are most probably due to the lack of dust self-heating in our code and the lower spatial resolution of the 3D calculations compared to the 1D ones. Since the geometry of the source emission/opacity of star/dust shell does not reproduce that for which our algorithm was developed, namely that of an extended distribution of stellar emission and dust, we also used a second benchmark. Thus, we considered the 2D calculations by P11 for the RFED distribution within their galaxy model. We calculated the contribution to the RFED distribution due to an old stellar disc and a young stellar disc separately and we compared the results for radial and vertical RFED profiles derived for a set of reference radii and vertical distances. We found a general good agreement between the 3D and 2D calculations within a few per cent in most of the cases. At least part of the residual discrepancy can be accounted by the relatively low spatial resolution of the grid used in the 3D calculation, which is not sufficient to properly resolve the thin disc component of the galaxy model of P11. We showed an example of a 3D application of the code by performing RT for a spiral galaxy model where in one case the emissivity of the young stellar population and associated dust opacity are distributed in logarithmic spiral arms and in another case are distributed in exponential discs. We found that the edge-on images, the attenuation as a function of inclination and the azimuthally average RFED profiles on the galaxy plane are approximately the same for the two models. This suggests that the spatially integrated SEDs of spirals can be well described by 2D models.

The tests we performed have shown that, in the conditions where dust self-heating is negligible and the 3D spatial resolution is high enough to resolve emission and opacity distributions, our code can be used to calculate accurate solutions for the RFED. This characteristic is particularly important for the calculation of stochastically heated dust emission, which requires both the overall intensity and the colour of the radiation field to be calculated in an accurate way.

In a future work we will show applications of the code for the calculation of infrared emission. This will be performed using our 3D RT code coupled with the dust emission code used by P11, which self-consistently calculates the stochastic emission from small grains and PAH molecules. In this way, it will be possible to use our code to obtain both integrated SEDs and images in the MIR and FIR for galaxies with arbitrary geometries. In addition, an important step will be to further optimize the code in order to make it possible to run on grids containing millions of cells in a reasonably short time. This will allow us to improve further the accuracy of the calculation for RFED within multiscale structures spanning at least three orders of magnitude, such as from ≈ 10 pc to ≈ 10 kpc in the case of a galaxy ISM.

ACKNOWLEDGEMENTS

We acknowledge support from the UK Science and Technology Facilities Council (STFC; grant ST/J001341/1). GN thanks S. Dalla, K. Foyle, E. Kafexhiu, T. Laitinen, J. Steinacker for useful suggestions and/or discussions. CCP thanks the Max Planck Institute für Kernphysik for support during a sabbatical, when this work was completed.

REFERENCES

- Abel T., Wandelt B. D., 2002, *MNRAS*, 330, 53
 Baes M., Verstappen J., De Looze I., Fritz J., Saftly W., Vidal Pérez E., Stalevski M., Valcke S., 2011, *ApJS*, 196, 22
 Bendo G. J. et al., 2012, *MNRAS*, 419, 1833
 Bianchi S., 2008, *A&A*, 490, 461
 Bianchi S., Ferrara A., Giovanardi C., 1996, *ApJ*, 465, 127
 Bisbas T. G., Bell T. A., Viti S., Yates J., Barlow M. J., 2012, *MNRAS*, 427, 2100
 Chakrabarti S., Whitney B. A., 2009, *ApJ*, 690, 1432
 Dale D. A. et al., 2007, *ApJ*, 655, 863
 Dale D. A. et al., 2012, *ApJ*, 745, 95
 Draine B. T., Li A., 2007, *ApJ*, 657, 810
 Driver S. P., Popescu C. C., Tuffs R. J., Liske J., Graham A. W., 2007, *MNRAS*, 379, 1022
 Driver S. P., Popescu C. C., Tuffs R. J., Graham A. W., Liske J., Baldry I., 2008, *ApJ*, 678, 101
 Driver S. P. et al., 2012, *MNRAS*, 427, 3244
 Dullemond C. P., Turolla R., 2000, *A&A*, 360, 1187
 Efstathiou A., Rowan-Robinson M., 1990, *MNRAS*, 245, 275
 Ercolano B., Barlow M. J., Storey P. J., 2005, *MNRAS*, 362, 1038
 Fischer O., Henning Th., Yorke H. W., 1994, *A&A*, 284, 187
 Gordon K. D., Misselt K. A., Witt A. N., Clayton G. C., 2001, *ApJ*, 551, 269
 Górski K. M., Hivon E., Banday A. J., Wandelt B. D., Hansen F. K., Reinecke M., Bartelmann M., 2005, *ApJ*, 622, 759
 Grootes M. W. et al., 2013, *ApJ*, 766, 59
 Guhathakurta P., Draine B. T., 1989, *ApJ*, 345, 230
 Gunawardhana M. L. P. et al., 2011, *MNRAS*, 415, 1647
 Hummer D. G., Rybicki G. B., 1971, *MNRAS*, 152, 1
 Ivezic Z., Elitzur M., 1997, *MNRAS*, 287, 799
 Ivezic Z., Groenewegen M. A. T., Men'shchikov A., Szczerba R., 1997, *MNRAS*, 291, 121 (197)
 Jonsson P., 2006, *MNRAS*, 372, 2
 Kylafis N. D., Bahcall J. N., 1987, *ApJ*, 317, 637
 Kuiper R., Klahr H., Dullemond C., Kley W., Henning T., 2010, *A&A*, 511, 81
 Mattila K., 1970, *A&A*, 9, 53
 Misiriotis A., Kylafis N. D., Papamastorakis J., Xilouris E. M., 2000, *A&A*, 353, 117
 Misiriotis A., Popescu C. C., Tuffs R., Kylafis N. D., 2001, *A&A*, 372, 775

- Odenwald S., Newmark J., Smoot G., 1998, *ApJ*, 500, 554
 Pascucci I., Wolf S., Steinacker J., Dullemond C. P., Henning Th., Niccolini G., Woitke P., Lopez B., 2004, *A&A*, 417, 793
 Popescu C. C., Tuffs R. J., 2002, *MNRAS*, 335, 41
 Popescu C. C., Tuffs R. J., 2013, *MNRAS*, 436, 1302 (PT13)
 Popescu C. C., Misiriotis A., Kylafis N. D., Tuffs R. J., Fischera J., 2000, *A&A*, 362, 138
 Popescu C. C., Tuffs R. J., Völk H. J., Pierini D., Madore B. F., 2002, *ApJ*, 567, 221
 Popescu C. C., Tuffs R. J., Dopita M. A., Fischera J., Kylafis N. D., Madore B. F., 2011, *A&A*, 536, 138 (P11)
 Roark T., Roark B., Collins G. W., II, 1974, *ApJ*, 190, 67
 Robitaille T. P., 2011, *A&A*, 536, 79
 Rowan-Robinson M., 1980, *ApJS*, 44, 403
 Schechtman-Rook A., Bershady M. A., Wood K., 2012, *ApJ*, 746, 70
 Semionov D., Vansevicius V., 2005, *Balt. Astron.*, 14, 543
 Semionov D., Vansevicius V., 2006, *Balt. Astron.*, 15, 601
 Semionov D., Kodaira K., Stonkut R., Vansevicius V., 2006, *Balt. Astron.*, 15, 581
 Siebenmorgen R., Kruegel E., Mathis J. S., 1992, *A&A*, 266, 501
 Silva L. et al., 2011, *MNRAS*, 410, 2043
 Sodroski T. J., Odegard N., Arendt R. G., Dwek E., Weiland J. L., Hauser M. G., Kelsall T., 1997, *ApJ*, 480, 173
 Steinacker J., Henning Th., Bacmann A., Semenov D., 2003, *A&A*, 401, 405S
 Steinacker J., Baes M., Gordon K., 2013, *ARA&A*, 51, 63
 Xilouris E. M., Kylafis N. D., Papamastorakis J., Paleologou E. V., Haerendel G., 1997, *A&A*, 325, 135
 Xilouris E. M., Alton P. B., Davies J. I., Kylafis N. D., Papamastorakis J., Trewhella M., 1998, *A&A*, 331, 894
 Xilouris E. M., Byun Y. I., Kylafis N. D., Paleologou E. V., Papamastorakis J., 1999, *A&A*, 344, 868
 Weingartner J. C., Draine B. T., 2001, *ApJ*, 548, 296
 Witt A. N., 1977, *ApJS*, 35, 1
 Witt A. N., Gordon K. D., 1996, *ApJ*, 463, 681
 Witt A. N., Stephens T. C., 1974, *AJ*, 79, 948
 Witt A. N., Thronson H. A., Jr, Capuano J. M., Jr, 1992, *ApJ*, 393, 611

This paper has been typeset from a $\text{\TeX}/\text{\LaTeX}$ file prepared by the author.